Finite element analysis and design method of geosynthetic-reinforced soil foundation subjected to normal fault movement

Jung Chiang [a], Kuo-Hsin Yang [a,*], Yu-Hsuan Chan [a], Chung-Lu Yuan [b]

[a] Department of Civil Engineering, National Taiwan University (NTU), 1, Sec. 4, Roosevelt Rd., Taipei 106, Taiwan
[b] Sinotech Engineering Consultants, 171, Sec. 5, Nanking East Rd., Taipei 105, Taiwan

ARTICLE INFO

ABSTRACT

This paper presents a series of finite element analyses to investigate the performance and reinforcing mechanism of geosynthetic-reinforced soil (GRS) foundations subjected to normal fault movement. Numerical and experimental results of unreinforced and reinforced foundations were first compared for model validation. Parametric studies were then conducted to evaluate the influence of soil and reinforcement parameters on the performance of reinforced foundations. The total height of the baseline reinforced foundation was 3 m in the prototype scale, and this foundation was subjected to fault movement of up to 1 m ($S/H = 33\%$). The variables considered in the parametric studies included reinforcement length, stiffness, ultimate tensile strength, vertical spacing, foundation height, and soil–reinforcement interface property. The numerical results revealed that FE analysis satisfactorily predicted the deformation behavior of unreinforced and reinforced foundations subjected to normal fault movement. Two main reinforcing mechanisms identified in this study were tensioned membrane and shear rupture interception effects. Based on the numerical results, regression equations for predicting the maximum angular distortion and the mobilized reinforcement tensile strain induced by normal fault movement were established. Design methods were also developed for determining the reinforcement length (against significant pullout) and failure strain (against breakage).

1. Introduction

Fault-induced ground movement and surface ruptures have been identified as principal earthquake hazards. Four hazards associated with fault movement are as follows: (1) distinct surface fault rupture, (2) significant differential settlement or angular distortion, (3) development of tensile strain in soil, and (4) development of tension cracks (Anastasopoulos et al., 2007; Bray, 2001; Lazarte et al., 1994). These hazards exert extra shear forces or bending moments on the buildings or infrastructure overlying the fault movement area, which could cause severe damage to the structures and result in casualties. To avoid these devastating hazards, generally, construction of buildings or structures across or adjacent to an existing surface fault rupture should be avoided. Many countries have regulations to restrict the construction of buildings within site-specific fault setbacks. However, the strategy of avoidance is not usually viable for linear infrastructures such as highways, railways, roads, tunnels, and levees. In such cases, geotechnical measures should be implemented to mitigate the impact of fault movement and surface ruptures on the overlying infrastructures.

The related geotechnical measures are categorized into three main groups: (1) installation of special foundations, (2) construction of embedded retaining walls or buffer trenches, and (3) placement of ductile engineering fills. The first group of geotechnical measures involves the use of rigid and continuous foundations (e.g., thick mat foundation or post-tensioned slabs) to maintain the foundations under rigid-body movement, thereby limiting structural distortion (Garcia and Bray, 2019a; 2019b; Rasouli and Fatahi, 2019; Oettle and Bray, 2013; Anastasopoulos et al., 2009; Bray, 2009; Faccioli et al., 2008; Gazetas et al., 2008). The second group of geotechnical measures involves the use of embedded retaining walls (e.g., diaphragm walls, soil-bentonite mixtures, cofferdam structures, skirted foundations, or ground improvement of soil beneath a foundation) to divert the propagation of the shear rupture beyond the boundaries of the foundation (Loli et al., 2018; Ashtiani et al., 2017; Fadaee et al., 2016; Oettle and Bray, 2013) or the use of buffer trenches (e.g., seismic gaps or trenches filled with compressible clay, lightweight expanded clay aggregate [LECA], or expanded polystyrene [EPS]) to provide spaces to accommodate fault-induced ground movement. The third group of geotechnical measures involves the use of ductile engineering fills, which are often reinforced

---

* Corresponding author.
  E-mail addresses: d06521003@ntu.edu.tw (J. Chiang), khyang@ntu.edu.tw (K.-H. Yang).

Nomenclature

Basic SI units are given in parentheses

E_{50}^{ref}	secant modulus (kN/m^2)
E_{oed}^{ref}	tangent oedometer loading modulus (kN/m^2)
E_{ur}^{ref}	unloading–reloading modulus (kN/m^2)
c'	effective cohesion (kPa)
D_r	relative density (%)
H	foundation height (m)
J_{50}	reinforcement stiffness (kN/m)
L	total length (m)
L_l	fault influence length (m)
L_R	reinforcement length (m)
N	number of reinforcement layers (dimensionless)
N	scaling factor (dimensionless)
R^2	coefficient of determination (dimensionless)
R_{inter}	interface reduction factor (dimensionless)
S	fault offset (m)
S_v	reinforcement vertical spacing (m)
T_{max}	mobilized maximum reinforcement tensile force (kN/m)
T_{ult}	reinforcement ultimate tensile strength (kN/m)
x	distance to the left boundary (m)
z	depth of reinforcement layer (m)
σ_3	confining pressure (kPa)
σ_d	deviatoric stress (kPa)
α	dip angle of normal fault (°)
β_{allow}	allowable angular distortion (dimensionless)
β_{max}	maximum angular distortion (dimensionless)
$\beta_{p,max}$	maximum angular distortion of primary settlement (dimensionless)
$\beta_{s,max}$	maximum angular distortion of secondary settlement (dimensionless)
γ	soil unit weight (kN/m^3)
γ_{xy}	soil shear strain (dimensionless)
δ	surface settlement (m)
ε_a	soil axial strain (%)
ε_f	reinforcement tensile strain at failure (%)
ε_{max}	mobilized maximum reinforcement tensile strain (%)
ε_v	soil volumetric strain (%)
τ_{max}	soil-reinforcement interface shear strength (kPa)
$\tau_{mobilized}$	mobilized interface shear stress (kPa)
τ_{rel}	interface shear stress ratio (dimensionless)
ϕ'	effective peak friction angle (degree)
ϕ_{ps}	soil friction angle in the plane strain state (degree)
ϕ_{tx}	soil friction angle obtained by triaxial tests (degree)
ψ	dilation angle (degree)
σ_n	normal stress on the soil-reinforcement interface (kPa)

with geosynthetics, to diffuse the underlying fault movement over a wider zone; this reduces angular distortion at the ground surface and thus maintains the stability of the overlying structures (Ashtiani et al., 2017; Bray, 2009; Bray, 2001; Lazarte et al., 1994; Bray et al., 1993). Among the three groups of geotechnical measures, the effectiveness and performance of the first two groups are significantly affected by the relative location between the geotechnical structures and the path of the shear rupture. However, the prediction of the shear rupture path is challenging because it is often associated with many geological uncertainties. The third group of measures that uses geosynthetics, which usually extends a long distance, could cover the potential surface fault rupture area; thus, these measures are more suitable than those in the first two groups for liner infrastructure. Moreover, the first two groups often require deep excavations to be to conducted and excavation support to be constructed, whereas the third group requires no or less excavation of soil.

Geosynthetics have been used to mitigate total or differential settlements in highway embankments with compressible soil, landfill liners founded on high-compressibility decomposed waste, and bridge abutments with foundation soil erosion (Marx and Jacobsz, 2018; Ardah et al., 2018; Talebi et al., 2017; Rajesh and Viswanadham, 2015; Kost et al., 2014; Miao et al., 2014; Jiang et al., 2012; Rajesh and Viswanadham, 2012; Stulgis et al., 1996). Studies have proven that geosynthetic-reinforced soil (GRS) structures exhibit high performance on yield foundations. Nevertheless, few studies have reported the use of geosynthetics to mitigate surface faulting problems. Bray (2001) and Bray et al. (1993) have conducted a series of finite element (FE) studies to evaluate the performance of the geosynthetic-reinforced earth fill for the mitigation of surface faulting hazards. In these studies, the FE models consisted of earth fills reinforced with 2–4 layers of geogrid subjected to normal fault movement up to 5 cm. The numerical results indicated that the geosynthetic reinforcement caused the effective spread of the fault-induced ground movement across a wider zone. Therefore, the angular distortion and soil tensile strain were sufficiently reduced to acceptable levels of risk. Moosavi and Jafari (2012) investigated the effect of geosynthetic reinforcement on mitigating reverse faulting hazards by using both physical tests and FE analyses. They also

found that the reinforced foundation could effectively reduce the angular distortion at the ground surface. Yang et al. (2020) conducted a series of reduced model tests to investigate the performance of GRS foundations subjected to normal fault movement. Experimental tests modeled a 3-m thick foundation (in the prototype) subjected to a fault displacement of up to 90 cm. The test results revealed that compared with unreinforced foundations, the reinforcement could effectively prevent the shear rupture from propagating upward to the ground surface, resulting in an average reduction of 60% in the angular distortion at the ground surface. Rasouli and Fatahi (2019) and Xu and Fatahi (2018) have performed FE analyses to assess the benefits of constructing a geosynthetic-reinforced cushioned pile foundation for surface faulting mitigation. These studies have proven that the inclusion of a geosynthetic-reinforced cushion layer between the raft and piles can modify dynamic structural characteristics and the load transfer mechanism and thus improve the geotechnical and structural performance of foundations and buildings (e.g., by reducing raft rocking and permanent structural inter-story drifts).

Geosynthetics have been applied in engineering practice to mitigate surface faulting hazards. An extension of a highway was constructed in central Taiwan, with a section planned to cross the Chelungpu fault (Fig. 1). Vertical surface movement of the Chelungpu fault reached 2–4 m in the Chi-Chi earthquake ($M_L = 7.3$) in 1999 (Chen et al., 2001). Past failure experiences have shown that rigid gravity-type retaining walls could not withstand large fault-induced surface ruptures. The final decision in this highway extension project was to build a ductile highway embankment with a GRS structure across the surface fault rupture zone. The GRS structure consisted of a GRS wall and an underlying GRS foundation (Fig. 1). The GRS wall was constructed to accommodate the differential settlement and maintain the stability and serviceability of the highway embankment, whereas the GRS foundation was adopted to enhance the bearing capacity of the foundation soil and to reduce the extent of the fault-induced angular distortion to an acceptable level. This study focused on the effect of the GRS foundation on mitigating fault-induced ground movement and surface ruptures.

Studies have demonstrated the geosynthetic-reinforced fill or GRS foundations as a valid measure to mitigate surface faulting hazards.

(a)

Purpose of GRS wall:
to accommodate the differential settlement
and maintain the stability and serviceability
of the highway embankment

Backfill

Drainage

GRS wall

Ground surface

Reinforcement

GRS foundation

Bedrock

Fault

Purpose of GRS Foundation:
to enhance the bearing capacity of the
foundation soil and reduce the fault induced
angular distortion (focus of this study)
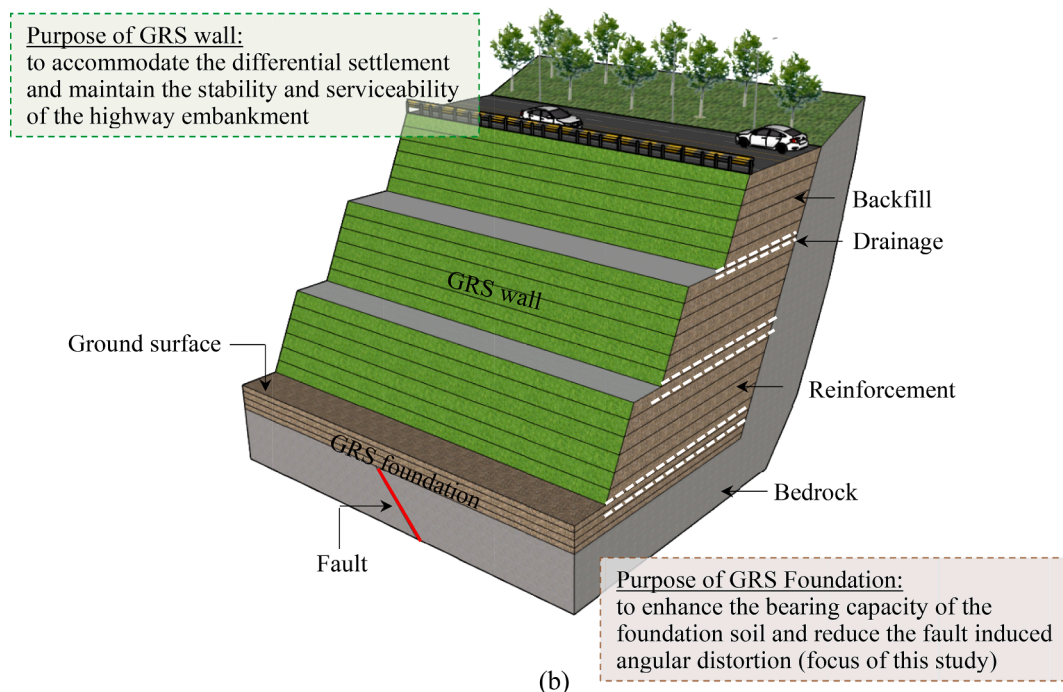
(b)

Fig. 1. GRS structures constructed in central Taiwan as a highway embankment to mitigate hazards associated with surface fault rupture: (a) photo during construction; (b) schematic illustration.

However, the influence of soil and reinforcement parameters on the performance of GRS foundations has not been fully studied. Furthermore, the design methods of GRS foundations to predict the maximum angular distortion and prevent reinforcement breakage and pullout have not been reported. Thus, in this study, a series of FE analyses were conducted to investigate the performance and reinforcing mechanism of GRS foundations subjected to normal fault movement. The specific study objectives were to 1) evaluate the effect of soil and reinforcement parameters on the performance of reinforced foundations; 2) investigate the reinforcing mechanism of geosynthetics; 3) establish the correlation regressions for the prediction of the maximum ground angular distortion and mobilized reinforcement tensile strain; and 4) propose design methods for reinforcement against breakage and pullout. In this paper, FE and numerical models are first introduced. The numerical models

were validated by comparing the numerical results with the model test results of Yang et al. (2020). After model validation, a series of parametric studies were conducted to evaluate the influence of soil and reinforcement parameters on the performance of reinforced foundations. Based on the parametric study results, multiple regression analyses were performed to establish regression equations for predicting the maximum angular distortion and mobilized reinforcement tensile strain under various soil and reinforcement parameters and fault displacement. Design methods were developed for determining the reinforcement length (against significant pullout) and failure strain (against breakage). The findings and discussion presented later in this paper provide valuable information for engineers to optimize the design of GRS foundations for the mitigation of surface faulting hazards.
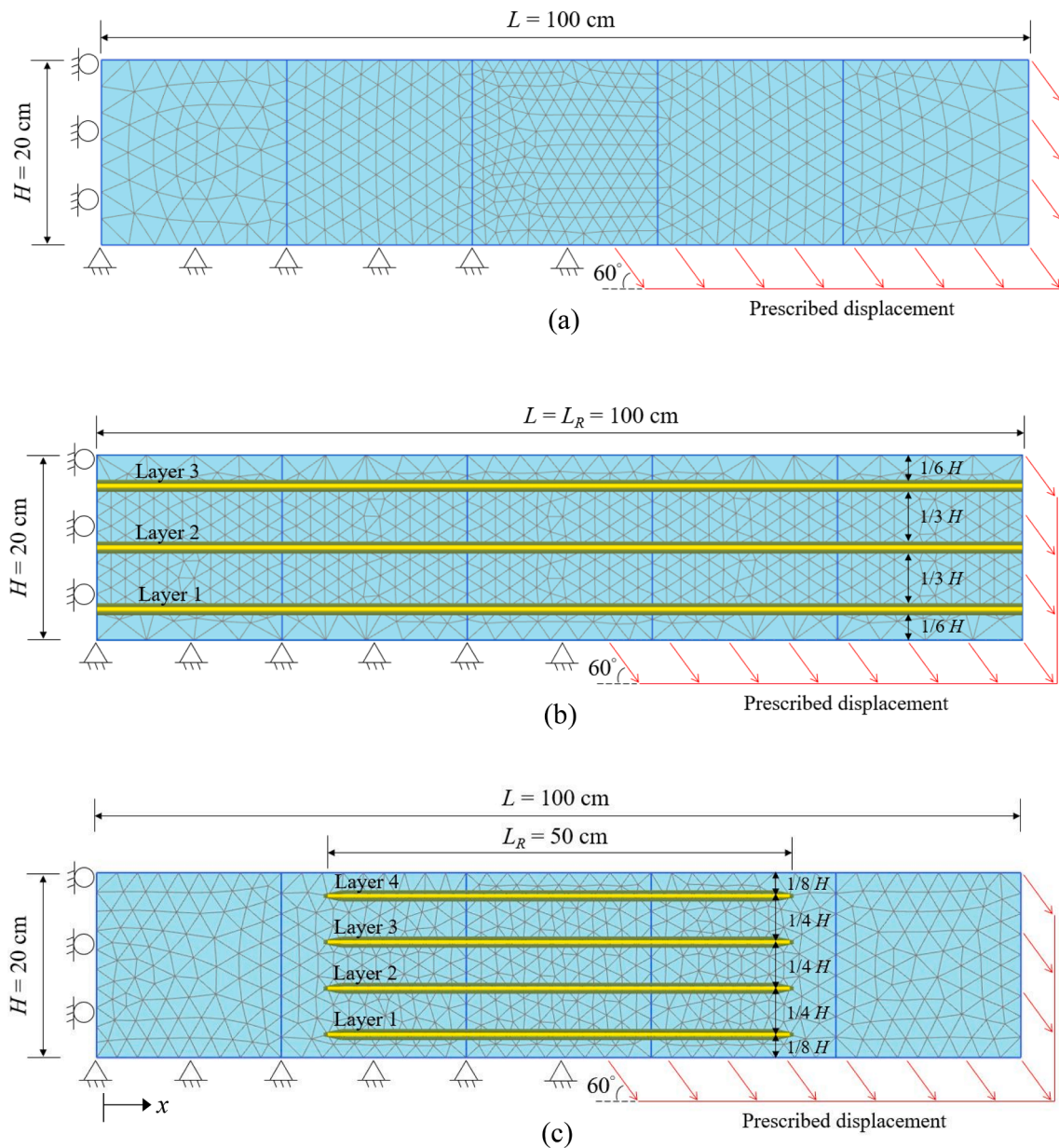
3

Fig. 2. Numerical models for model validation: (a) unreinforced foundation; (b) reinforced foundation; (c) reinforced foundation with short reinforcement.

Table 1
Input soil properties for model validation.

Properties	Values	
	Triaxial test	Plane strain
Soil index property		
Soil unit weight, γ (kN/m³)	15.3	15.3
Stiffness properties		
Secant modulus, E_{50}^{ref} (kN/m²)	45,000	101,250
Tangent oedometer loading modulus, E_{oed}^{ref} (kN/m²)	45,000 [a]	101,250 [a]
Unloading-reloading modulus, E_{ur}^{ref} (kN/m²)	135,000 [b]	303,750 [b]
Strength properties		
Effective friction angle, ϕ' (°)	39	42
Effective cohesion, c' (kPa)	0	0
Dilation angle, ψ (°)	9 [c]	12 [c]

[a] assumed to be 1 E_{50}^{ref} for granular soil.

[b] assumed to be 3 E_{50}^{ref} for granular soil.

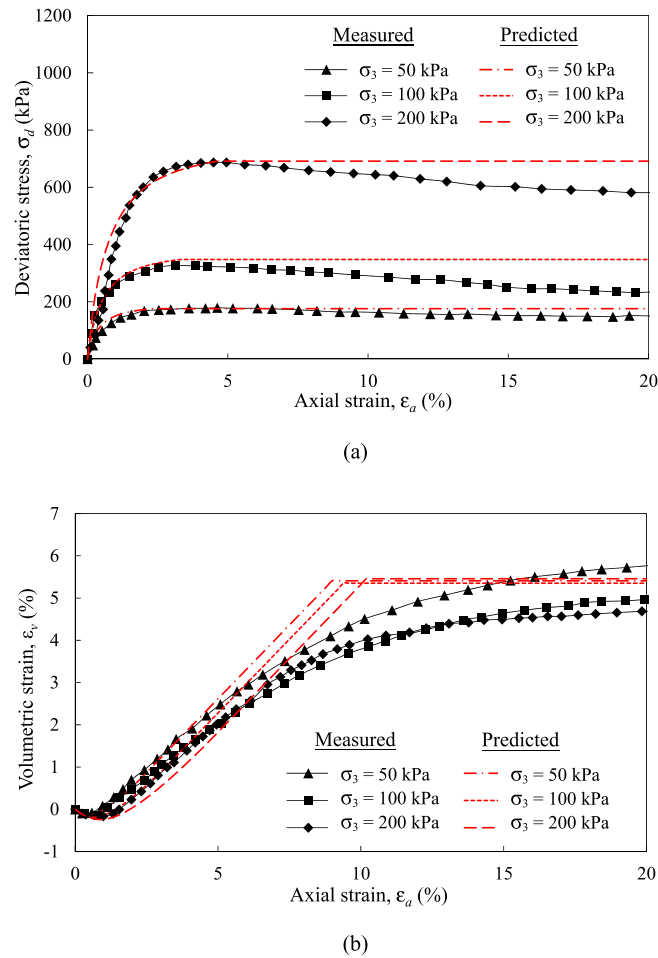[c] estimated by $\psi = \phi - 30°$ (Bolton, 1986).

(a)

(b)

Fig. 3. Calibration of soil parameters using triaxial test results: (a) deviatoric stress vs. axial strain; (b) volumetric strain vs. axial strain.

Table 2
Input reinforcement and soil-reinforcement interface properties.

Properties	Scaling factor [a]	Values	
		Reduced scale [b]	Prototype [c]
Reinforcement			
Ultimate tensile strength, T_{ult} (kN/m)	$1/N^2$	0.70	157.5
Stiffness, J_{50} (kN/m)	$1/N^2$	5.47	1231
Failure strain, ε_f (%)	1	12.7	12.7
Soil-Reinforcement Interface			
Interface reduction factor, R_{inter}	1	0.9	0.9

[a] target scaling factor $N = 15$.
[b] used in model validation.
[c] used in parametric study.

2. Numerical model and validation

This section presents three experimental and numerical models. The predicted and measured results, including surface settlement profile, maximum angular distortion, and maximum reinforcement tensile strain, were compared for model validation. The shear rupture propagation and reinforcing mechanism of the reinforcement are discussed in detail.

2.1. Numerical model and boundary conditions

Two-dimensional numerical models were developed under plane strain conditions by using the FE software PLAXIS (Brinkgreve et al., 2019). Numerical models were established to simulate three reduced scale models: unreinforced foundation, reinforced foundation, and reinforced foundation with short reinforcement (Fig. 2a–c). The numerical and experimental results were compared for model validation. The reduced model test results of Yang et al. (2020) for unreinforced and reinforced foundations were adopted, and the reduced model test of the reinforced foundation with short reinforcement was conducted in this study. This test used the same soil and reinforcement materials and followed the same test procedures and conditions as those of Yang et al. (2020).

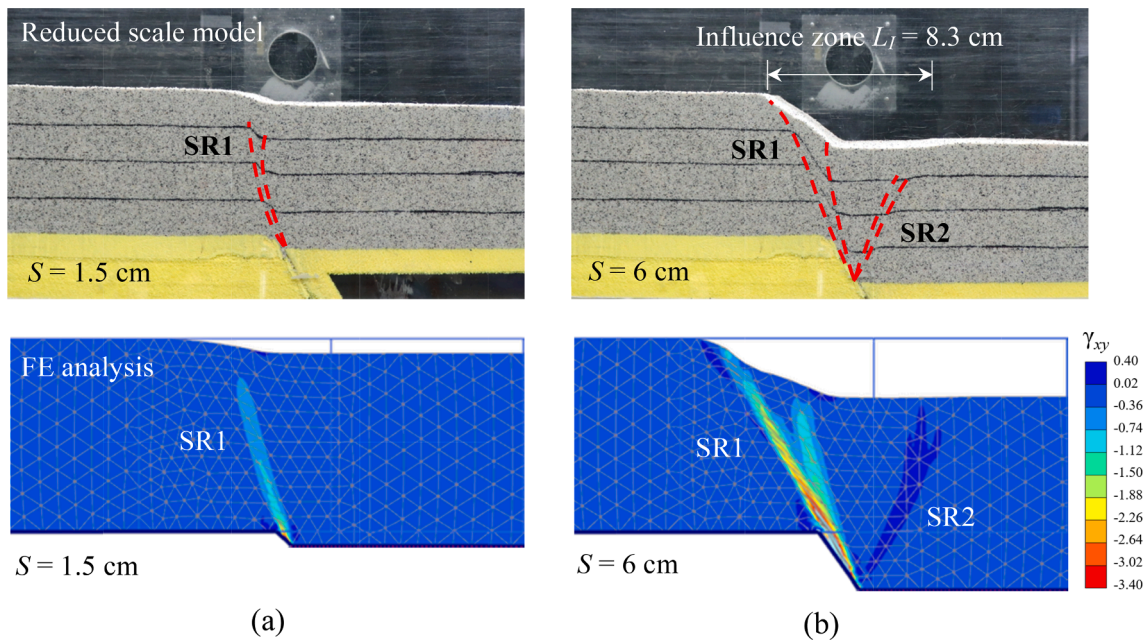The dimensions and layout of the numerical model are identical to

Fig. 4. Experimental and numerical results of the unreinforced foundation: (a) $S = 1.5$ cm; (b) $S = 6$ cm.
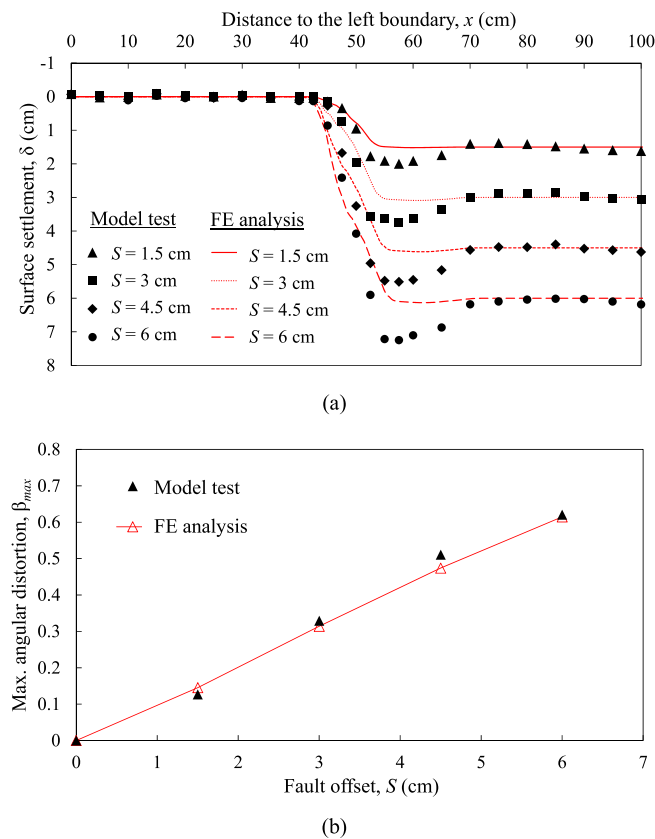

Fig. 5. Comparison of (a) ground surface settlement profile; (b) maximum angular distortion for the unreinforced foundation.

those of the reduced model test. The dimensions of the experimental test and numerical model are 100 cm × 20 cm ($L \times H$). A 15-node triangular element with 12 stress points is designated as the soil element, and a 5-node geogrid element with five stress points is assigned as reinforcement. Fine-element meshes are specified for the areas that may affected by the shear rupture propagation and soil–reinforcement interaction, whereas medium-element meshes are applied to the remaining areas. The assigned mesh density generates approximately 1500 triangular elements for a given geometry. The reinforced foundation has three reinforcement layers ($n = 3$), with the reinforcement length fully
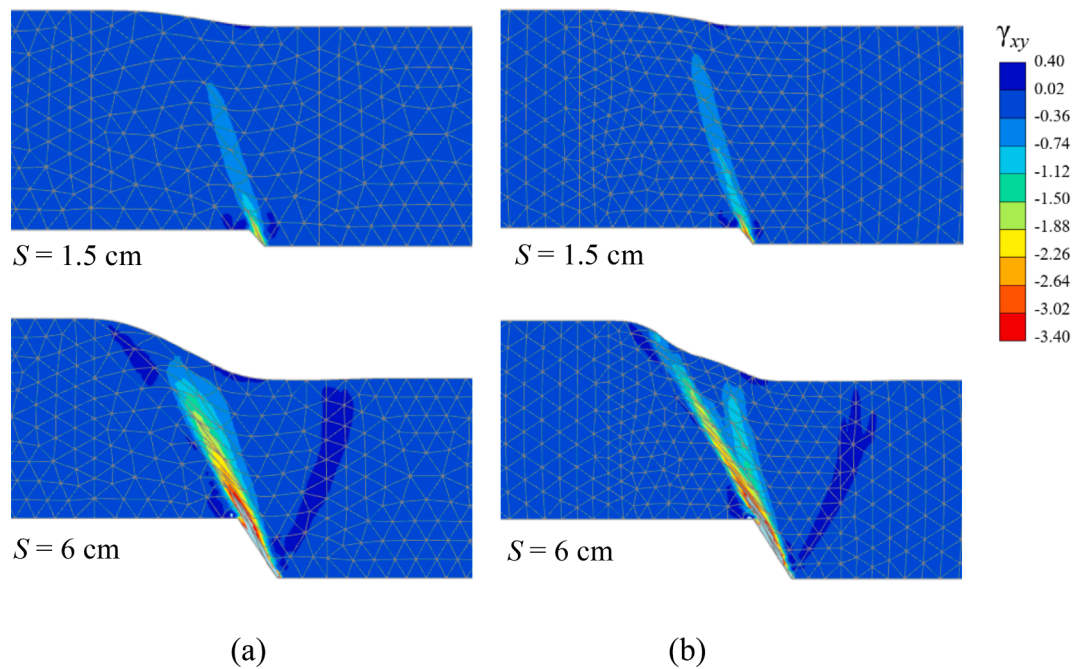
Fig. 6. Influence of mesh size on the numerical results of unreinforced foundations: (a) medium-element mesh (mesh size $\approx$ 2 cm); (b) fine-element mesh (mesh size $\approx$ 1.5 cm).
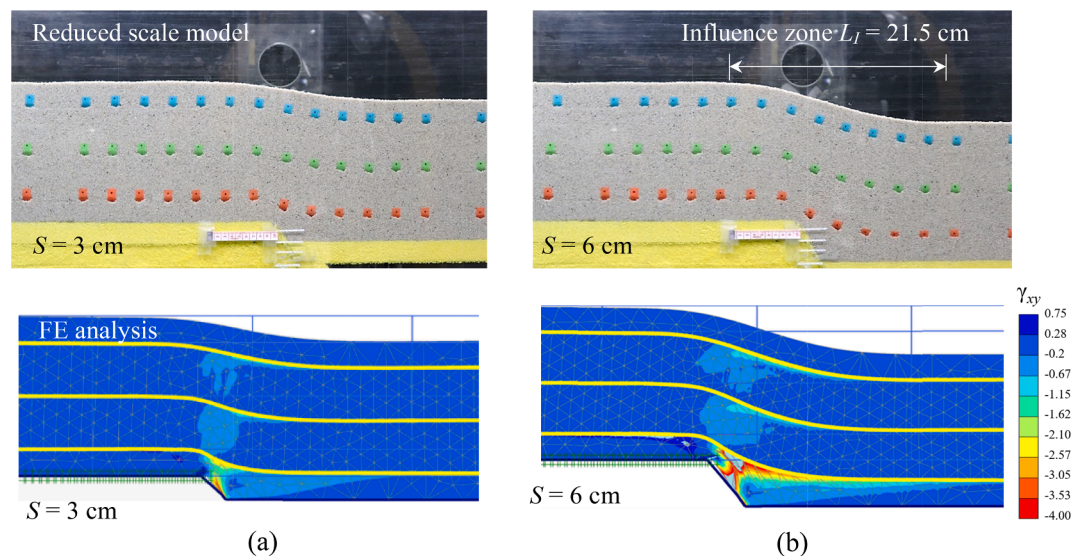

Fig. 7. Experimental and numerical results of the reinforced foundation: (a) $S = 3$ cm; (b) $S = 6$ cm.

extended to two ends of the model ($L_R = 100$ cm). The reinforced foundation with short reinforcement has four reinforcement layers ($n = 4$), with the reinforcement length only covering half of the model length ($L_R = 50$ cm). The reinforcement layers in the reinforced foundation are placed with uniform vertical spacing. The interface elements are applied along each reinforcement layer to simulate the soil–reinforcement interaction and to capture reinforcement pullouts that could occur in reinforced foundations with an insufficient reinforcement length.

In the initial phase, standard fixities are applied to the boundaries of the model. The left and right boundaries can move only in the vertical direction (i.e., $u_x = 0$, $u_y \neq 0$), whereas the bottom boundary is restrained from movement (i.e., $u_x = 0$, $u_y = 0$). The initial stress state is generated by the K_0 procedure in the initial phase. The vertical stress is in equilibrium with the self-weight of the soil, whereas the horizontal

stress is calculated from the specified value of K_0. The use of K_0 procedure can be justified because the foundation soil is confined by the sandbox. After the generation of the initial stress state, the displacement is reset to zero at the start of the calculation phases (i.e., prescribed displacement phases).

In the calculation phases, the prescribed displacement is applied to the right and bottom boundaries of the hanging wall to simulate 60° dip normal fault movement. The fault tip is located in the middle of the model (i.e., $x = 50$ cm). The maximum fault offset is up to $S = 6$ cm ($S/H = 30\%$), which is equivalent to 90 cm in the prototype, based on similitude laws of the reduced model tests conducted by Yang et al. (2020). Large deformation effects are considered in numerical analyses by selecting updated mesh and arc-length functions. In addition, to avoid numerical divergence, the increment of the prescribed displacement in each calculation phase is set to be very small (i.e., 2% of the
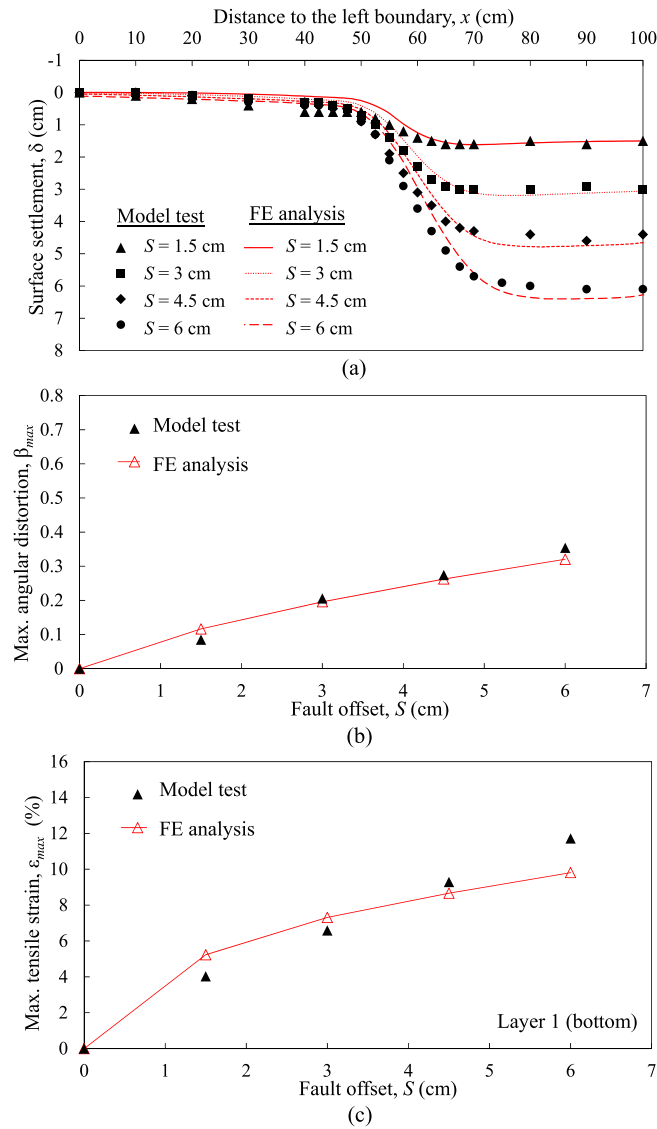
Fig. 8. Comparison of (a) ground surface settlement profile; (b) maximum angular distortion; (c) maximum reinforcement tensile strain at Layer 1 for the reinforced foundation.

maximum fault offset).

2.2. Input material properties

Table 1 presents a summary of the input soil properties for model validation. The soil used in the reduced model tests conducted by Yang et al. (2020) was uniform quartz sand, which is classified as poorly graded sand (SP) according to the Unified Soil Classification System (USCS). The soil is modeled as stress-dependent, hyperbolic, elasto-plastic material by using the hardening soil model (Schanz et al., 1999)). The input properties of the soil shear strength and soil modulus are first calibrated from consolidated-drained triaxial compression tests. Fig. 3 shows the calibration results of a comparison of the measured and predicted stress–strain–volumetric strain curves. To account for plane strain conditions in reduced model tests, the soil plane strain properties deduced from empirical correlations are input into the FE simulations in this study (Table 1). The soil plane strain friction angle is estimated using the following equation proposed by Lade and Lee (1976).

$$\phi_{ps} = 1.5 \ \phi_{tx} - 17 \tag{1}$$

where ϕ_{ps} (=42°) is the soil plane strain friction angle, and ϕ_{tx} (=39°) is

the soil triaxial compression friction angle. Allen et al. (2003) also adopted the same approach to convert ϕ_{tx} into ϕ_{ps} for calculating the mobilized reinforcement tensile forces within GRS walls. Studies have found that the soil dilatation angle influences the characteristics and paths of shear rupture propagation, which consequently affects fault-induced deformation at the ground surface (Anastasopoulos et al., 2007; Garcia and Bray, 2019a; 2019b). Therefore, the soil dilatation angle ψ is considered in this study. The input value of ψ (=12°) is estimated based on the empirical relationship (i.e., $\psi = \phi' - 30°$) proposed by Bolton (1986). Regarding the soil modulus, Marachi et al. (1981) reported that the soil plane-strain modulus is higher than the soil triaxial compression modulus for the same material under the same minor principal stress conditions. Hatami and Bathurst (2006) compared the data from triaxial compression and plane strain tests on Royal Military College (RMC) sand and reported that the ratio of the soil modulus from the plane strain test results to that from the triaxial compression test results is approximately 2.25. Because the quartz sand analyzed in this study and the RMC sand have similar shear strength properties, the same ratio was adopted in this study to estimate the soil plane stain modulus in FE simulations.

Table 2 presents a summary of the input reinforcement and soil–reinforcement interface properties for model validation. The
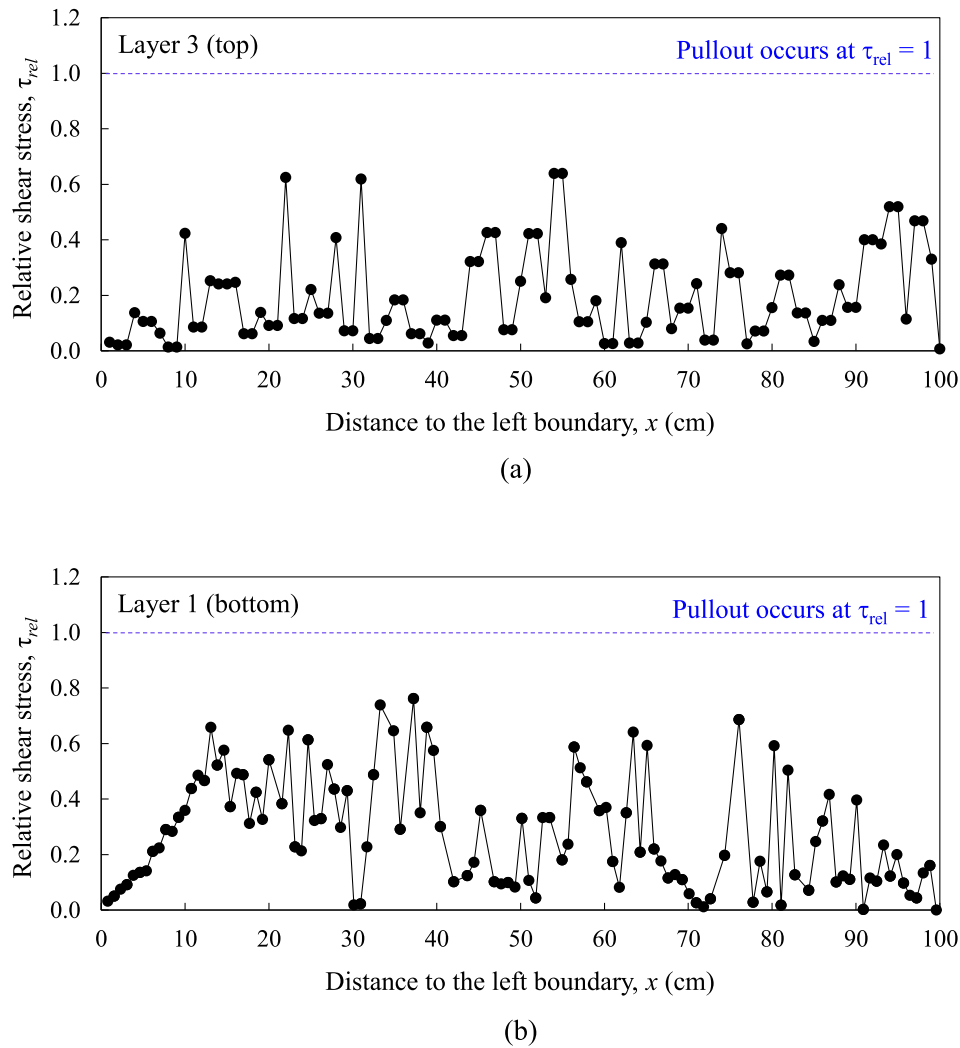
Fig. 9. Soil-reinforcement interface shear stress distribution of the reinforced foundation at $S = 6$ cm: (a) Layer 3; (b) Layer 1.

reinforcement used in reduced model tests is nonwoven polypropylene geotextile, which is modeled as a linear elastic–perfectly plastic geogrid element in FE analyses. The selected reinforcement model is superior to the linear or nonlinear elastic model commonly used for reinforcement because the mobilization of reinforcement tensile force can be set at a limited value (i.e., ultimate reinforcement tensile strength, T_{ult}). If the mobilized tensile force of a reinforcement layer reaches T_{ult} during the simulation, the reinforcement layer is manually deactivated to simulate reinforcement breakage. In this study, the input values of T_{ult} (=0.7 kN/m) and reinforcement stiffness J_{50} (=5.47%) are directly calibrated from the wide-width tensile test result of Yang et al. (2020). Notably, low input values are used for tensile properties because the reinforcement tensile strength and stiffness properties for 1 g model tests must be scaled down to $1/N^2$ of prototype tensile properties based on similitude laws. Table 2 lists the values of the scaling factor ($N = 15$) and corresponding tensile properties in the prototype.

The soil–reinforcement interface is modeled as a linear elastic–perfectly plastic interface element. The soil–reinforcement interface shear strength τ_{max} is defined by the Mohr–Coulomb failure criterion, expressed as

$$\tau_{max} = R_{inter} \times \sigma_n \tan\phi' \tag{2}$$

where R_{inter} is the interface reduction coefficient, σ_n is the normal stress acting on the soil–reinforcement interface, and ϕ' is the soil effective friction angle. $R_{inter} = 0.9$ is assumed for the sand–geotextile interface

based on the typical interface efficiency factor suggested by Yang et al. (2019). The interface shear stress ratio τ_{rel} is defined as

$$\tau_{rel} = \frac{\tau_{mobilized}}{\tau_{max}} \tag{3}$$

where $\tau_{mobilized}$ is the mobilized interface shear stress, and τ_{max} is the interface shear strength as defined in Eq. (2). Reinforcement pullout occurs when the mobilized interface shear stress reaches the interface shear strength (i.e., $\tau_{rel} = 1$).

2.3. Model validation and reinforcing mechanisms

2.3.1. Unreinforced foundation
Fig. 4 shows the experimental and numerical results of the unreinforced foundation subjected to normal fault displacement (i.e., free field conditions). The shear strain contour obtained from FE analyses reveals that the first shear rupture SR1 gradually propagates upward from the fault tip to the ground surface at $S = 3$ cm (Fig. 4a). SR1 reaches the ground surface at $S = 6$ cm (Fig. 4b). A distinct surface fault rupture occurs due to the breakthrough of SR1, producing a clear fault scarp at the ground surface. Moreover, the second/antithetic shear rupture SR2 is developed in the hanging wall. A gravity graben bordered by SR1 and SR2 begins to form. In general, the predicted shear rupture propagation and ground deformation characteristics of the unreinforced foundation are in good agreement with the measured results.
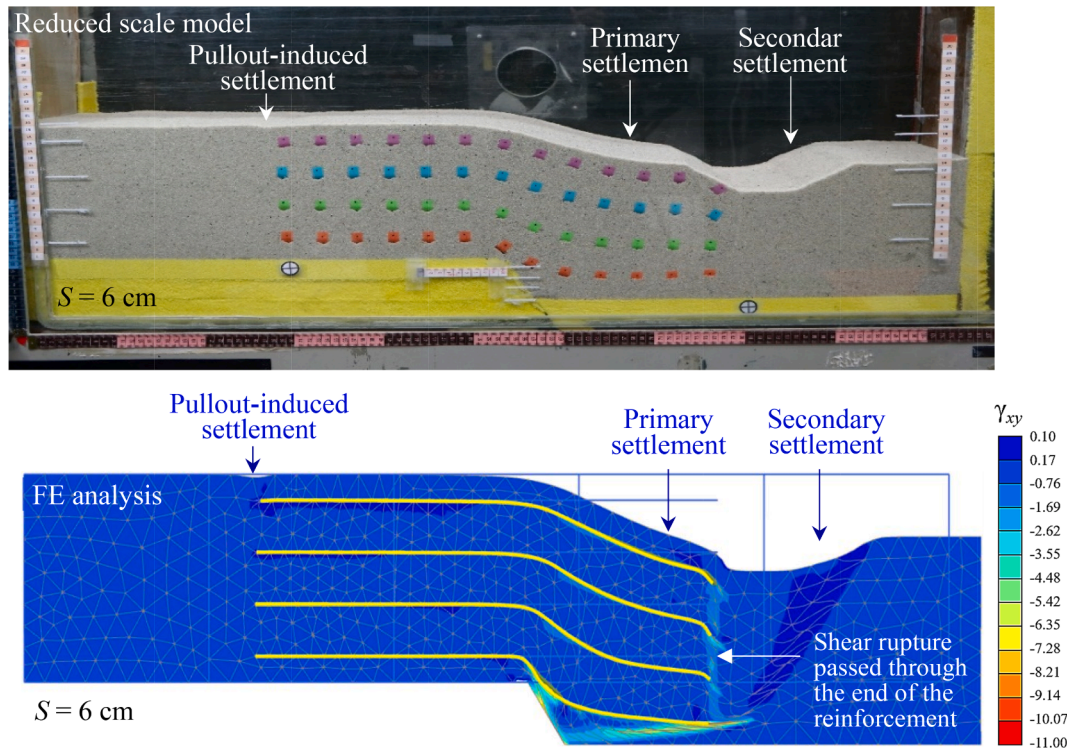
Fig. 10. Experimental and numerical results of the reinforced foundation with short reinforcement at $S = 6$ cm: (a) reduced scale model; (b) FE analysis.

Fig. 5a presents a comparison of the predicted and measured ground surface settlement profiles of the unreinforced foundation. The predicted and measured results are generally in good agreement, except that the surface settlement at the graben is underestimated in FE analyses. Garcia and Bray (2019a) reported a more localized settlement in the experiment than the predicted settlement in numerical analyses because the numerical mesh is inevitably larger than the real soil particle size; a thicker shear band and a less localized settlement are obtained in numerical analyses than in the experiment. Fig. 6 demonstrates the influence of mesh size on the numerical results of the unreinforced foundation. The numerical results reveal that the width of the shear bands induced by bedrock fault movement was affected by the mesh size of the numerical model. Thicker shear bands were observed as medium-element mesh was used in the FE analysis (Fig. 6a), whereas relatively narrow shear bands were obtained when fine-element mesh was adopted (Fig. 6b). Besides, more localized settlement profile can be observed from the numerical model with fine-element mesh. These numerical results agree with the observation reported in Garcia and Bray (2019a).

Fig. 5b shows a comparison of the maximum angular distortion β_{max} in the predicted and measured results at the ground surface for the unreinforced foundation. The angular distortion caused by the ground differential settlement is calculated using the following formula:

$$\beta_{ij} = \frac{\delta_{ij}}{l_{ij}} \tag{4}$$

where δ_{ij} is the differential settlement between the reference points i and j, and l_{ij} is the distance between i and j. The maximum angular distortion β_{max} is calculated as the maximum value of β along the ground surface, which also represents the steepest slope of the ground settlement profile. As shown in Fig. 5b, FE analysis accurately predicts β_{max} values at different fault offsets. Because the angular distortion critically influences the serviceability and damage of superstructures, the β_{max} value is used a key indicator for evaluating the performance of the reinforced foundation in this study.

2.3.2. Reinforced foundation

Fig. 7 presents the experimental and numerical results of the reinforced foundation subjected to normal fault movement. Compared with the distinct surface fault rupture observed for the unreinforced foundation, a gradual and smooth surface settlement profile is observed for the reinforced foundation in both experimental and numerical results. A graben is not formed in the reinforced foundation. Moreover, the reinforced foundation has a wider fault-induced influence zone than the unreinforced foundation (as indicated in Figs. 5 and 7), suggesting that the differential settlement is spread across a wider zone in the reinforced soil; this results in a reduction of the angular distortion at the ground surface. This reinforcing mechanism is identified as the tensioned membrane effect, in which the tensile force of the reinforcement is mobilized with fault displacement, and the vertical component of the mobilized tensile force supports the overlying soil and minimizes the impact from the surface settlement (King et al., 2019; Holtz et al., 1998; Giroud et al., 1990). Furthermore, the shear strain contours obtained from FE analyses reveal that the reinforcement effectively intercepts shear rupture propagation and prevents the rupture from propagating to the ground surface (Fig. 7). This reinforcing mechanism is identified as the shear rupture interception effect. Notably, due to this interception effect, the intense shear strain contour develops horizontally and extends along the bottom reinforcement layer (i.e., Layer 1). The developed shear strain fades with the increased distance from the fault tip, indicating that the energy of fault movement is progressively dissipated by the resistance provided by the soil–reinforcement interaction. In summary, the aforementioned two reinforcing mechanisms exerted by the reinforcement could effectively prevent the surface fault rupture and could significantly reduce the fault-induced angular distortion at the ground surface.

Fig. 8 presents a comparison of the predicted and measured ground surface settlement profiles, β_{max}, and the maximum reinforcement tensile strain ε_{max} in reinforcement Layer 1 for the reinforced foundation. The predicted surface settlement profile and β_{max} show good agreement with the measured results (Fig. 8a and 8b). The predicted ε_{max} values are slightly overestimated under a small S but are slightly underestimated
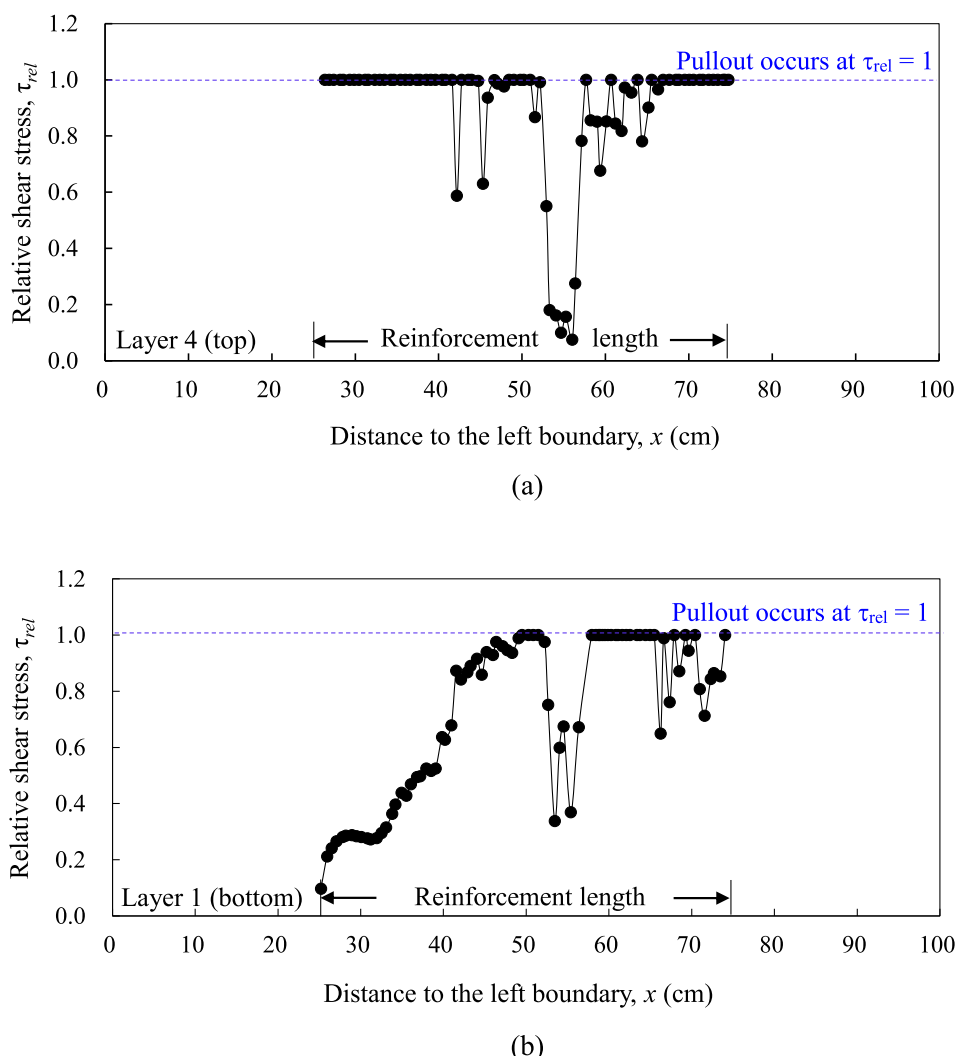
Fig. 11. Soil-reinforcement interface shear stress distribution of the reinforced foundation with short reinforcement at $S = 6$ cm: (a) Layer 4; (b) Layer 1.

under a large S (Fig. 8c). The reason of this discrepancy is that the reinforcement is modeled as a linear elastic–perfectly plastic material, and secant stiffness at 50% stress level J_{50} is input as a representative value for reinforcement stiffness. Because the actual reinforcement load–strain curve is nonlinear, the simulated reinforcement stiffness is lower than the actual stiffness under low-strain conditions; thus, ε_{max} is overestimated under a small S in FE analyses. Similarly, the simulated reinforcement stiffness is higher than the actual stiffness under high-strain conditions; thus, ε_{max} is underestimated under a large S in FE analyses. Fig. 9 shows the soil–reinforcement interface shear stress distributions of the reinforced foundation. Fig. 9 indicates that $\tau_{rel} < 1.0$ along the reinforcement layer, indicating that no reinforcement pullout occurred for the reinforced foundation with sufficient reinforcement length.

2.3.3. Reinforced foundation with short reinforcement

Fig. 10 displays the experimental and numerical results of the reinforced foundation with short reinforcement subjected to normal faulting. Due to the insufficient reinforcement length, the shear rupture first develops horizontally along reinforcement Layer 1 and then propagates vertically to the ground surface through the end of the reinforcement. In addition to the primary settlement, a secondary settlement occurs due to the propagation of a shear rupture to the ground surface (Fig. 10). The measured and predicted surface settlement profiles and the corresponding β_{max} value (=0.428 at $S = 6$ cm) are in reasonably good

agreement.

Fig. 11 shows the soil–reinforcement interface shear stress distributions of the reinforced foundation with short reinforcement to examine the mechanism of reinforcement pullout. For the top reinforcement layer (i.e., Layer 4), reinforcement pullout occurs (i.e., $\tau_{rel} = 1$) in the both hanging wall and footwall due to the relatively low interface shear strength because of the low overburden pressure acting in this layer. (Fig. 11a). In the hanging wall (the right part of the reinforced foundation), reinforcement pullout is caused by the loss of reinforcement anchorage due to the passage of the shear rupture at the end of the reinforcement. In the footwall (the left part of the reinforced foundation), reinforcement pullout is driven by the mobilization of the reinforcement tensile force with fault displacement. As indicated in Fig. 8, reinforcement pullout in the hanging wall induces a secondary settlement, and reinforcement pullout in the footwall also induces a slight pullout-induced settlement. For the bottom reinforcement layer (i.e., Layer 1), reinforcement pullout only occurs for the reinforcement embedded in the hanging wall because of the development of the intense interface shear stress due to the passage of the shear rupture along this layer (Fig. 11b).

In summary, FE analyses could satisfactorily predict the ground deformation characteristics of the unreinforced and reinforced foundations subjected to normal fault movement. For the reinforced foundation with short reinforcement, FE analyses could also capture the primary and secondary settlements caused by reinforcement pullout. The model

Table 3
Numerical program and results of parametric study.

Group	Parameters	Reinforcement length L_R (m)	Reinforcement stiffness J_{50} (kN/m)	Reinforcement ultimate tensile strength T_{ult} (kN/m)	Parameters Reinforcement vertical spacing S_v (m)	Foundation height H (m)	Interface reduction factor R_{inter}	Results [a],[b] Maximum angular distortion at primary settlement $\beta_{p,\max}$	Maximum angular distortion at secondary settlement $\beta_{s,\max}$	Maximum mobilized tensile strain ε_{max} (%)
Baseline case		25	1000	150	1	3	0.9	0.386	0	11.22
Reinforcement	Reinforcement length	5	1000	150	1	3	0.9	0.509	0.393	5.07
		10						0.393	0.189	9.59
		15						0.393	0.097	11.10
		20						0.388	0.041	11.25
		25						0.386	0	11.22
	Reinforcement stiffness	10	500	150	1	3	0.9	0.436/0.426	0.184/0	15.13/15.38
		25	1000					0.393/0.386	0.189/0	9.59/11.22
			1500					0.378/0.365	0.305/0.03	7.03/9.23
	Reinforcement ultimate tensile strength	10	1000	50	1	3	0.9	0.416/0.525	0.212/0	5/5 [c]
		25		80				0.422/0.421	0.212/0	8/8 [c]
				150				0.393/0.386	0.189/0	9.59/11.22
				200				0.393/0.386	0.189/0	9.59/11.22
	Reinforcement vertical spacing	10	1000	150	0.75	3	0.9	0.383/0.373	0.194/0	8.64/10.75
		25			1			0.393/0.386	0.189/0	9.59/11.22
					1.5			0.466/0.466	0/0	8.59/10.59
Soil	Foundation height	10	1000	150	1	2	0.9	0.419/0.419	0.482/0.043	6.98/9.10
		25				3		0.393/0.386	0.189/0	9.59/11.22
						4		0.346/0.338	0.158/0	11.48/12.68
						6		0.276/0.273	0.135/0	13.44/14.01
Interface	Interface reduction factor	10	1000	150	1	3	0.67	0.415/0.401	0.216/0.027	9.12/10.76
		25					0.9	0.393/0.386z	0.189/0	9.59/11.22
							1.0	0.379/0.367	0.021/0	9.72/11.25

[a] test results at $S = 1.0$ m.
[b] values before and after slash are for the cases of $L_R = 10$ m and 25 m, respectively.
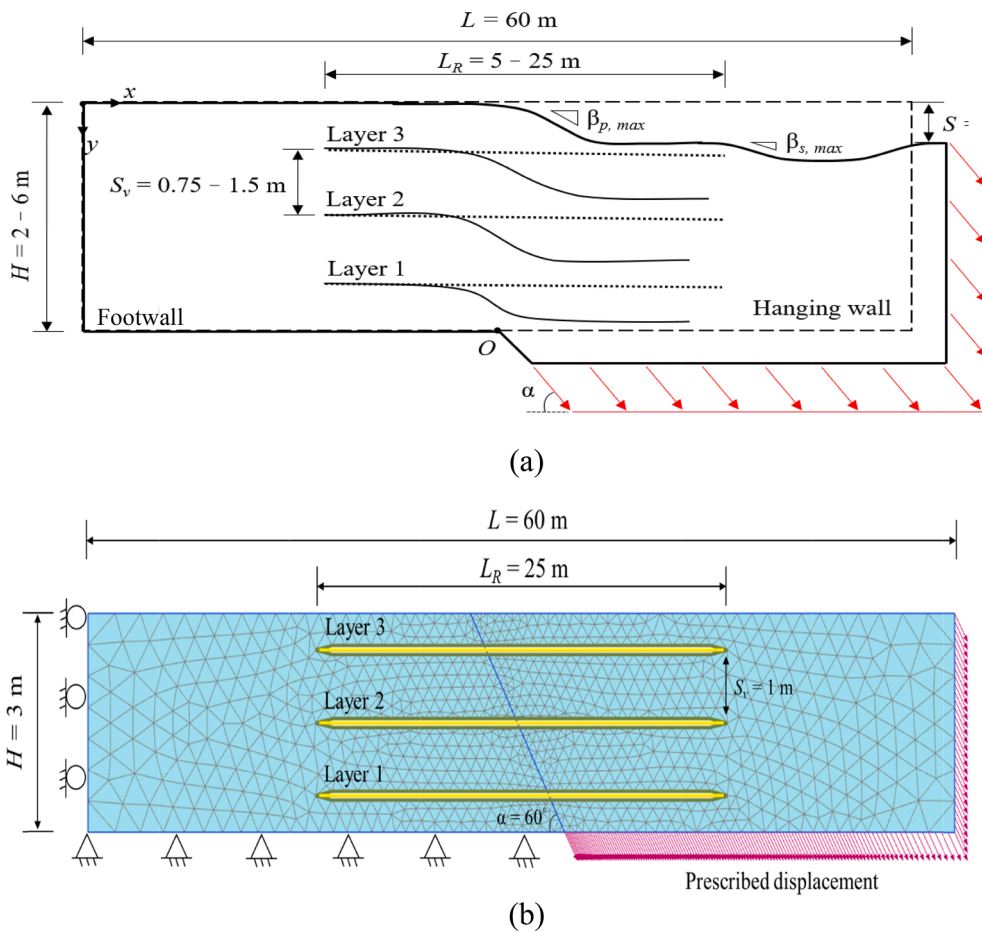[c] reinforcement breakage

12

Fig. 12. Numerical model used in the parametric study: (a) illustration; (b) numerical model of the baseline case (not in scale).

validation results demonstrate that the FE analysis established in this study is appropriate for investigating the performance of GRS foundations subjected to normal fault movement.

3. Parametric study

A series of parametric studies of the full-scale reinforced foundation was conducted to evaluate the influence of soil and reinforcement parameters on the performance of the reinforced foundation. Table 3 lists the numerical program and results of the parametric study. The variables considered in the parametric study include the reinforcement length L_R, stiffness J_{50}, ultimate tensile strength T_{ult}, vertical spacing S_v, foundation height H, and soil–reinforcement interface reduction factor R_{inter}. It should be noted that the reinforcement spacing considered in the baseline case is $S_v = 1$ m, which is larger than the reinforcement spacing, for the conventional GRS wall, typically ranging from $S_v = 0.3$–0.6 m. It is because the GRS foundation and the GRS wall have different design functions and play different roles (as shown in Fig. 1). The reinforcement in the GRS foundation is mainly to reduce the fault-induced angular distortion at the ground surface, but the reinforcement in the GRS wall is to resist the lateral earth pressure and thus maintain the stability of the wall. Accordingly, the reinforcement spacing in the GRS foundation could be designed differently from the GRS wall. Fig. 12 shows the baseline numerical model used in the parametric study. The baseline case has dimensions of 60 m $\times 3$ m ($L \times H$) and three reinforcement layers with $L_R = 25$ m (Fig. 12b). The fault tip is located in the middle of the model (i.e., $x = 30$ m). The normal fault has a dip angle of $\alpha = 60°$, and S increases up to 1.0 m ($S/H = 33\%$). The settings of boundary conditions and large deformation effects are identical to the numerical model described in the model validation section. The prototype

reinforcement tensile properties are used in the parametric study (Table 2). As shown in Fig. 12a, the maximum angular distortions of the primary settlement $\beta_{p,max}$ and the secondary settlement $\beta_{s,max}$ are used as key performance indicators to evaluate the influence of each parameter.

3.1. Reinforcement length

Fig. 13 shows the influence of the reinforcement length on the ground surface settlement profile and β_{max} at various fault offsets. The reinforcement lengths considered are $L_R = 5$, 10, 15, 20, and 25 m. The unreinforced case ($L_R = 0$ m) is also plotted in Fig. 13 for reference. The numerical results show that the slope of the primary settlement becomes steep as S increases (Fig. 13a). In addition to the primary settlement, secondary and pullout-induced settlements are observed at $L_R < 25$ m. The numerical results also show that $\beta_{p,max}$ and $\beta_{s,max}$ decrease as L_R increases and S decreases (Fig. 13b). $\beta_{p,max}$ reaches a constant value at $L_R \geq 10$ m, and $\beta_{s,max}$ decreases to null at $L_R = 25$ m. For all cases, $\beta_{p,max}$ is higher than $\beta_{s,max}$. Because $\beta_{p,max}$ is more critical than $\beta_{s,max}$, the maximum angular distortion at the ground surface is governed by $\beta_{p,max}$ (i.e., $\beta_{max} = \beta_{p,max}$).

Investigation of the interface shear stress in the top reinforcement layer (i.e., Layer 3) shows that reinforcement pullout is associated with the $\beta_{s,max}$ value; thus, the $\beta_{s,max}$ value can be used as an indicator to identify reinforcement pullout. Reinforcement pullout does not occur at $L_R = 25$ m ($\beta_{s,max} = 0$), but it occurs to various degrees at $L_R < 25$ m as the fault offset increases ($\beta_{s,max} > 0$). Slight reinforcement pullouts develop in the cases of $L_R = 10$–20 m, which seem to have little impact on $\beta_{p,max}$. However, significant reinforcement pullout develops in the case of excessively short reinforcement (i.e., $L_R = 5$ m), which considerably diminishes reinforcing functions (i.e., tensioned membrane and
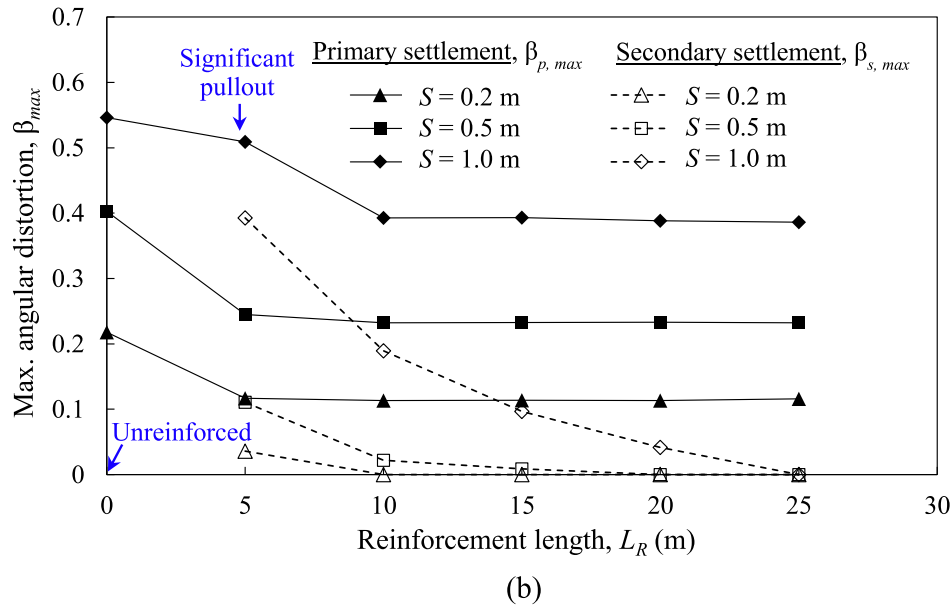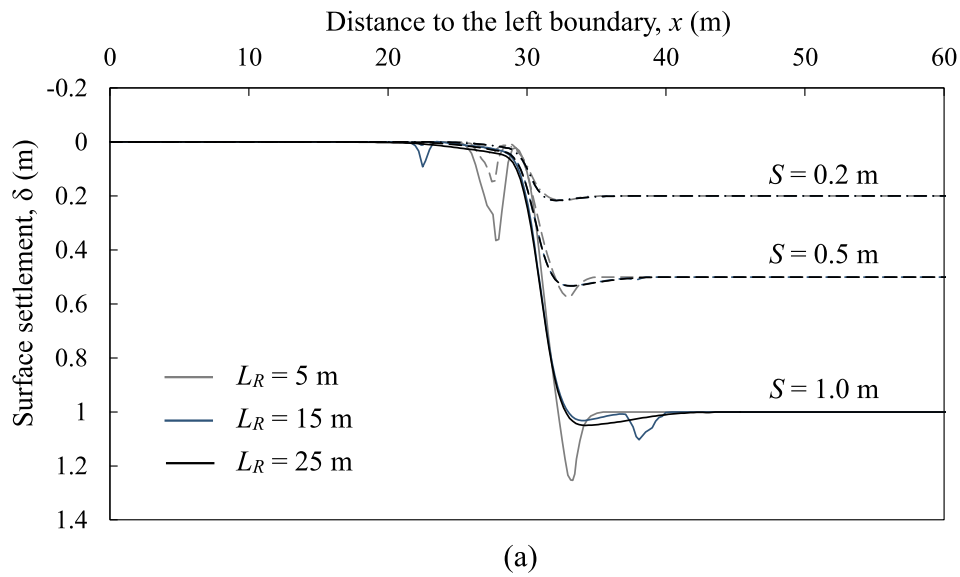
Fig. 13. Influence of reinforcement length on: (a) ground surface settlement profile; (b) maximum angular distortion.

shear rupture interception effects), resulting in high $\beta_{p,\max}$ and $\beta_{s,\max}$, especially at a large fault offset (Fig. 13b).

Fig. 14 shows the influence of the reinforcement length on the mobilized reinforcement tensile strain distribution and ε_{max} in reinforcement Layer 1. The numerical results show that the mobilized reinforcement tensile strain peaks at approximately above the fault tip, and the strain gradually decreases to zero with increasing distance from the fault tip (Fig. 14a). The ε_{max} value determined from the peak reinforcement tensile strain increases as L_R and S increases (Fig. 14b). ε_{max} reaches a constant value at $L_R \geq 15$ m because reinforcements are sufficiently long to provide sufficient anchorage for the development of the tensile strain. As the reinforcement is subjected to the tension induced by normal faulting, ε_{max} can be used to examine whether the reinforcement breaks as the fault offset increases. For the cases of $L_R \geq 15$ m, $\varepsilon_{max} \approx 11\%$ at $S = 1.0$ m. The mobilized ε_{max} value is still less than the reinforcement tensile strain at failure $\varepsilon_f = 12.7\%$ (Table 2), indicating that reinforcement breakage does not occur in these cases.

Fig. 15 displays the relationships between β_{max} and the total mobilized reinforcement tensile force ΣT_{max} at $S = 1.0$ m. The maximum reinforcement tensile force T_{max} for each reinforcement layer is calculated as

$$T_{max} = J_{50} \times \varepsilon_{max} \tag{5}$$

where J_{50} is the reinforcement secant stiffness, and ε_{max} is the mobilized maximum tensile strain in the reinforcement layer. ΣT_{max} is the sum of T_{max} of the three reinforcement layers in a reinforced foundation. In Fig. 15, $\beta_{p,\max}$ and ΣT_{max} appear to have a linear relationship, irrespective of different reinforcement lengths. This unique linear relationship confirms that the reinforcement exerts the tensioned membrane effect through the mobilization of the reinforcement tensile force to support the overlying soil, thus reducing β_{max} at the ground surface.
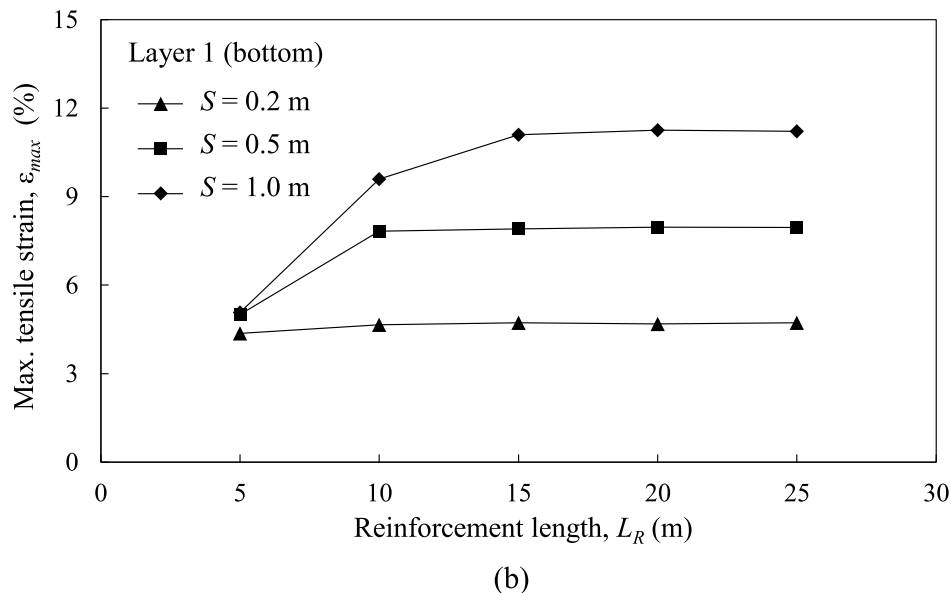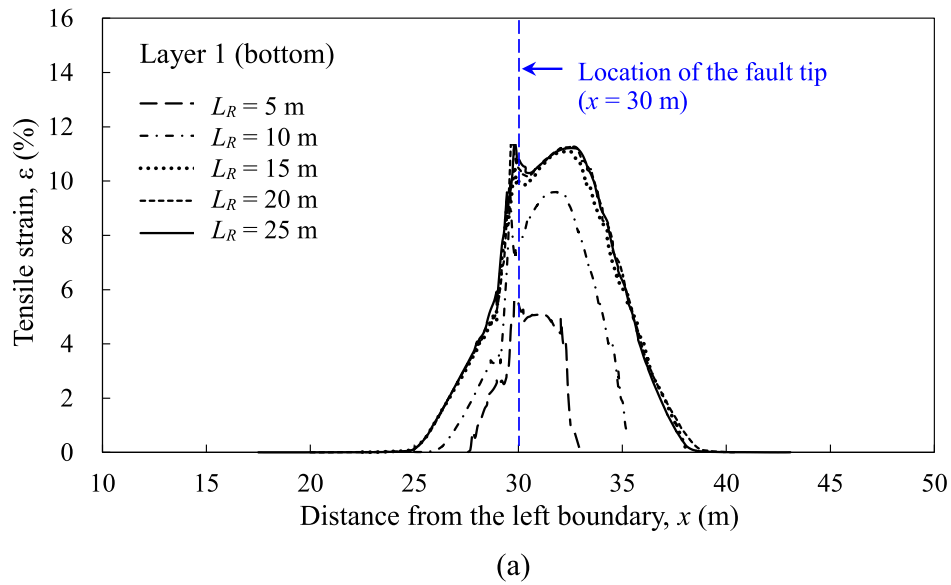
(a)

(b)

Fig. 14. Influence of reinforcement length on: (a) mobilized reinforcement tensile strain at $S = 1.0$ m; (b) maximum reinforcement tensile strain at Layer 1.

3.2. Reinforcement stiffness

Fig. 16 shows the influence of reinforcement stiffness on β_{max} and ε_{max} at $S = 1.0$ m. Reinforcement stiffness values are $J_{50} = 500$, 1000, and 1500 kN/m. Two reinforcement lengths ($L_R = 10$ and 25 m) are selected and evaluated. These two reinforcement lengths are selected based on the previous discussion of the development of various degrees of reinforcement pullout associated with different reinforcement lengths. The numerical results show that $\beta_{p,max}$ decreases as J_{50} increases, whereas the opposite trend is observed for $\beta_{s,max}$ (Fig. 16a). The numerical results also show that ε_{max} in reinforcement Layer 1 significantly decreases as J_{50} increases (Fig. 16b). The numerical results are supported by the results of model tests conducted by Yang et al. (2020), showing that low β_{max} and ε_{max} values in the foundation with stiff reinforcement. The decrease in ε_{max} with the increase in J_{50} is likely because the stiffer reinforcement deforms less under the same fault movement, resulting in a lower ε_{max} value. Nevertheless, T_{max} in the stiffer reinforcement is still higher. For example, under the condition of

$L_R = 25$ m at $S = 1$ m, $\varepsilon_{max} = 9.23\%$ and 15.38%, and the corresponding $T_{max} = 138.4$ and 76.9 kN/m (calculated using Eq. (5)) in the case of $J_{50} = 1500$ and 500 kN/m, respectively.

Stiff reinforcement, which produces a high T_{max} value, can generate a strong tensioned membrane effect and thus reduce $\beta_{p,max}$ at the ground surface. Moreover, the high T_{max} value produced from stiff reinforcement is a high driving force that increases the potential of reinforcement pullout and thus increases $\beta_{s,max}$ at the ground surface. Notably, $\beta_{s,max}$ is close to $\beta_{p,max}$ in the case of $J_{50} = 1500$ kN/m and $L_R = 10$ m. $\beta_{s,max}$ is likely to exceed $\beta_{p,max}$ and become critical if J_{50} further increases or L_R decreases.

3.3. Reinforcement ultimate tensile strength

Fig. 17 shows the influence of the reinforcement ultimate tensile strength on β_{max} and ε_{max} at $S = 1.0$ m. Reinforcement ultimate tensile strength values are $T_{ult} = 50$, 80, 150, and 200 kN/m. The numerical results show that $\beta_{p,max}$ and $\beta_{s,max}$ decrease (Fig. 17a) and that ε_{max} in
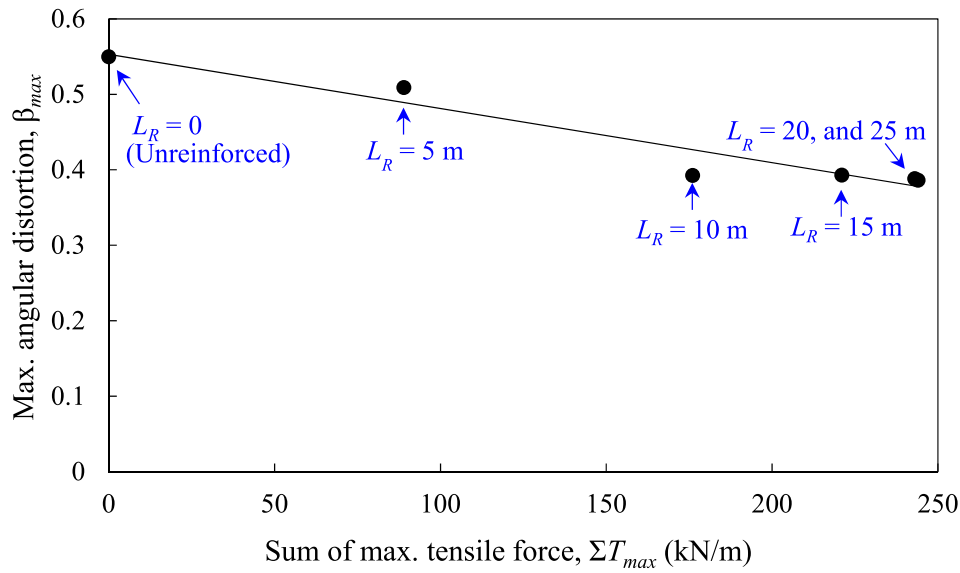
Fig. 15. Relationships between maximum angular distortion and sum of maximum reinforcement tensile force of the three reinforcement layers at $S = 1$ m.

reinforcement Layer 1 increases as T_{ult} increases (Fig. 17b). High β_{max} and low ε_{max} values in the foundation with weak reinforcement, as described in the earlier text, result from reinforcement breakage as fault displacement increases. Table 4 presents a summary of the corresponding fault offset during reinforcement breakage. Reinforcement breakage mainly occurs for the reinforcement with a low ultimate tensile strength ($T_{ult} = 50$ and 80 kN/m). In this reinforcement, the mobilization of ε_{max}, as shown in Fig. 17b, is limited by the reinforcement failure strain ($\varepsilon_f = 5\%$ and 8% for the cases of $T_{ult} = 50$ and 80 kN/m, respectively).

In the case of $T_{ult} = 50$ kN/m and $L_R = 25$ m, three reinforcement layers from the bottom to top are ruptured subsequently at $S = 0.2, 0.5,$ and 0.7 m, respectively. The ground surface settlement profiles at different fault offsets corresponding to the breakage of each reinforcement layer are shown in Fig. 18a. Due to the impact of reinforcement breakage, the reinforcing functions of all three reinforcement layers are lost. The final ground settlement profile at $S = 1$ m became similar to that of the unreinforced foundation (Fig. 18b). Consequently, the maximum angular distortion is $\beta_{max} = 0.52$ at $S = 1$ m, which is close to that of the unreinforced foundation ($\beta_{max} = 0.55$; Fig. 17a). In the case of $T_{ult} = 50$ kN/m and $L_R = 10$ m, reinforcement breakage occurs in the middle and bottom layers. Reinforcement pullout restrains the development of the maximum tensile force and thus prevents reinforcement breakage in the top layer. Notably, in the case of $T_{ult} = 50$ kN/m and $L_R = 10$ m, ruptures occur in the bottom two layers; only the top reinforcement layer could still effectively provide reinforcing function, therefore producing a $\beta_{p,max}$ value slightly higher than that of the cases of no reinforcement breakage (i.e., high reinforcement tensile strength), and the $\beta_{p,max}$ value is lower than the value for the case of complete reinforcement breakage (i.e., the case of $T_{ult} = 50$ kN/m and $L_R = 25$ m).

3.4. Reinforcement vertical spacing

Fig. 19 shows the influence of reinforcement vertical spacing on β_{max} and ε_{max} at $S = 1.0$ m. Reinforcement in these simulations have uniform vertical spacing, and S_v values are 0.75, 1, and 1.5 m, corresponding to the number of reinforcement layers are $n = 4, 3,$ and 1, respectively. The numerical results show that $\beta_{p,max}$ decreases as S_v decreases, whereas the opposite trend is observed for $\beta_{s,max}$ (Fig. 19a). The low $\beta_{p,max}$ value in the reinforced foundation with close-spaced reinforcement is as expected because more reinforcement layers could provide more reinforcing effects to reduce the angular distortion at the ground surface.

The high $\beta_{s,max}$ value in the reinforced foundation with short reinforcement and close reinforcement spacing (i.e., the cases of $L_R = 10$ m and $S_v = 0.75,$ and 1 m) is caused by reinforcement pullout due to insufficient anchorage length and low overburden pressure acting on the top reinforcement layers. The numerical results agree with the experimental results of reduced model tests conducted by Yang et al. (2020). The test results by Yang et al. (2020) found the 1-layer reinforced foundation had the largest β_{max} value. The test results also suggested that the 3-layer reinforced foundation had an optimal effect, further increase in reinforcement layers (or decrease in S_v) had a minor influence on β_{max}.

The numerical results also show that S_v has a minor effect on ε_{max} value. The ε_{max} values at the bottom reinforcement layer show no specific trend (Fig. 19b), which is counterbalanced by the effect of the number of reinforcement layers and the location of the bottom reinforcement layer. The reinforced foundation with close-spaced reinforcement has high system stiffness and thus could generate less internal deformation with the fault movement. Consequently, the low ε_{max} value is observed in this foundation. Besides, the ε_{max} value is also influenced by the reinforcement location. Notably, the ε_{max} value of the 1-layer reinforced foundation was lower than that of the 3-layer reinforcement foundation. It is because the ε_{max} value decreased as the distance between the reinforcement and bedrock fault increased. Because the reinforcement in the case of $S_v = 1.5$ m (i.e., $n = 1$) was placed at the middle of the foundation, a distance above the bedrock fault, the displacement boundary had less influence on reinforcement strain mobilization.

3.5. Foundation height

Fig. 20 shows the influence of the foundation height on β_{max} and ε_{max} at $S = 1.0$ m. Foundation height values are $H = 2, 3, 4,$ and 6 m. The numerical results show that $\beta_{p,max}$ and $\beta_{s,max}$ substantially decrease (Fig. 20a), and ε_{max} in reinforcement Layer 1 increases as H increases (Fig. 20b). The low β_{max} value in the thick foundation is because the thick soil layer has high bending stiffness to resist bending deformation due to the differential settlement. The high ε_{max} value in the thick foundation likely results from the strong soil–reinforcement interaction caused by the high overburden pressure acting on the bottom reinforcement layer. The numerical results in this study agree with the numerical results of FE analyses conducted by Bray (2001) and Bray et al. (1993) and the results of the model tests conducted by Yang et al. (2020). These studies found that the fill height is a controlling factor for
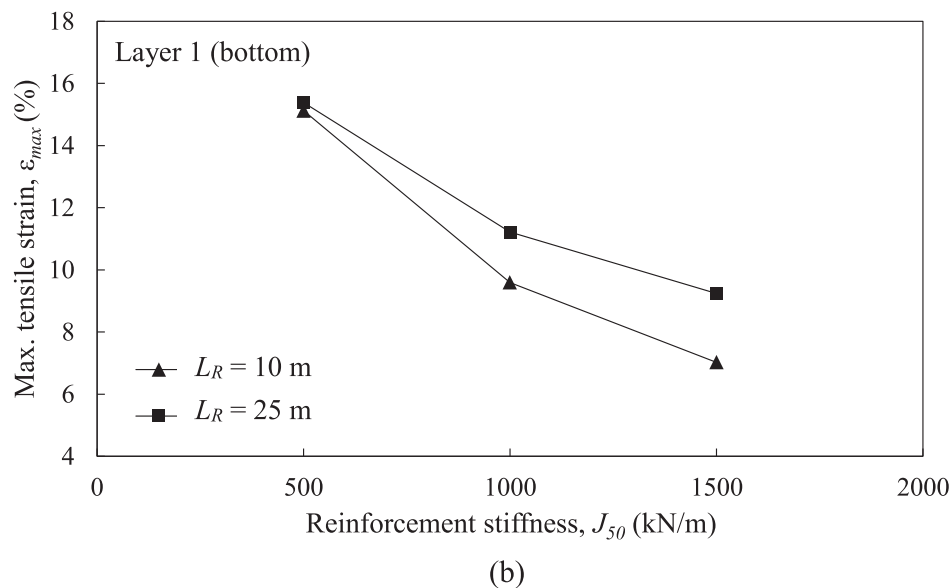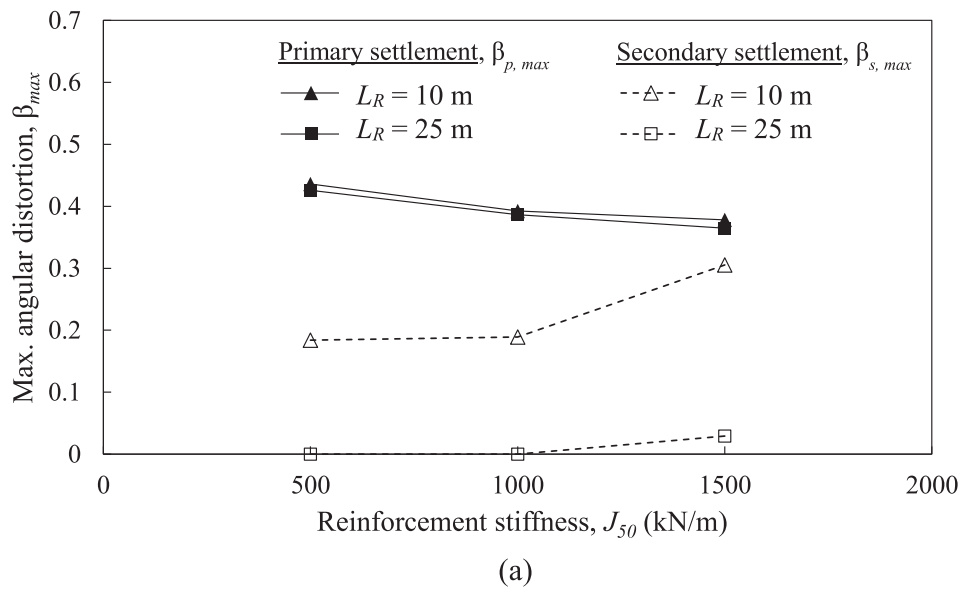
(a)

(b)

Fig. 16. Influence of reinforcement stiffness on: (a) maximum angular distortion; (b) maximum reinforcement tensile strain at Layer 1 at $S = 1.0$ m.

reducing the angular distortion at the ground surface. They attributed the observed trend to the thick soil foundation that could absorb more fault displacement.

In the case of $H = 2$ m and $L_R = 10$ m, both $\beta_{p,max}$ and $\beta_{s,max}$ increase due to the combined effects of high bending deformation and significant reinforcement pullout in the thin foundation. The significant pullout causes the $\beta_{s,max}$ (=0.48) value to become approximately equal to the $\beta_{p,max}$ (=0.49) value in the case of $H = 2$ m and $L_R = 10$ m. The pullout also occurs in the case of $H = 2$ m and $L_R = 25$ m as $\beta_{s,max} > 0$. As described in the earlier text, the design of a thin foundation should be avoided. Based on the numerical results, the foundation height should be at least three times larger than the anticipated normal fault offset (i.e., $S/H < 0.3$) to prevent the adverse effects of a thin foundation.

3.6. Soil–reinforcement interface property

Fig. 21 shows the influence of the soil–reinforcement interface property on β_{max} and ε_{max} at $S = 1.0$ m. The interface reduction factors,

as defined in Eq. (2), are $R_{inter} = 0.67, 0.9$, and 1.0. R_{inter} within the range of typical input values has a minor effect on β_{max} and ε_{max} values. $\beta_{p,max}$ and $\beta_{s,max}$ slightly decrease (Fig. 21a), and ε_{max} in reinforcement Layer 1 slightly increases as R_{inter} increases (Fig. 21b). Low β_{max} and high ε_{max} values were observed in the foundation with the strong interface property because the strong soil–reinforcement interaction produces a high T_{max} value, which generates a strong tensioned membrane effect and thus reduces β_{max} at the ground surface. Notably, pullout ($\beta_{s,max} > 0$) occurs in the case of $R_{inter} = 0.67$ and $L_R = 25$ m, which has sufficient long reinforcement but a relatively weak interface property.

3.7. Sensitivity assessment

Fig. 22 presents the sensitivity assessment results. The effect of each parameter on β_{max} and ε_{max} values is quantitatively compared using a sensitivity assessment. The x-axis in Fig. 22 represents the percentage change of input parameters, and the y-axis represents the percentage change in output values (i.e., β_{max} or ε_{max} at $S = 1$ m). The percentage
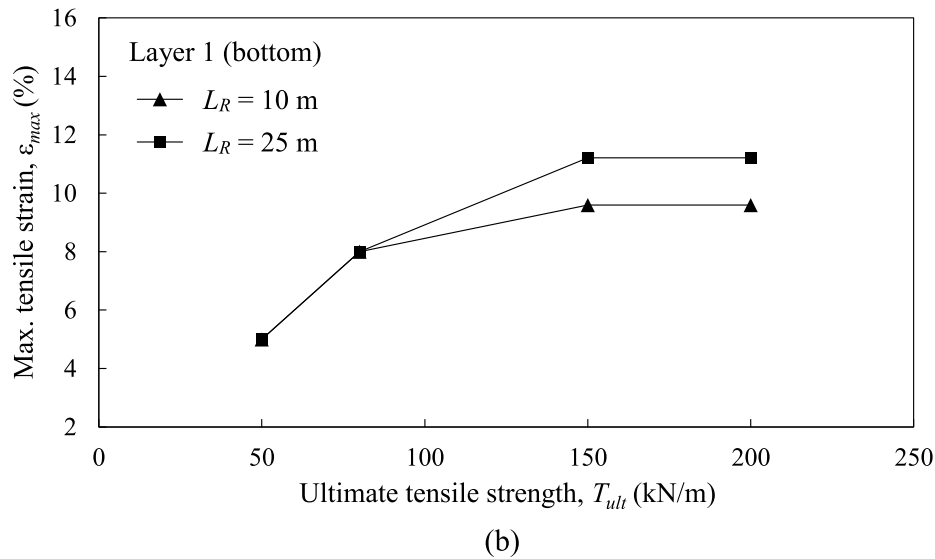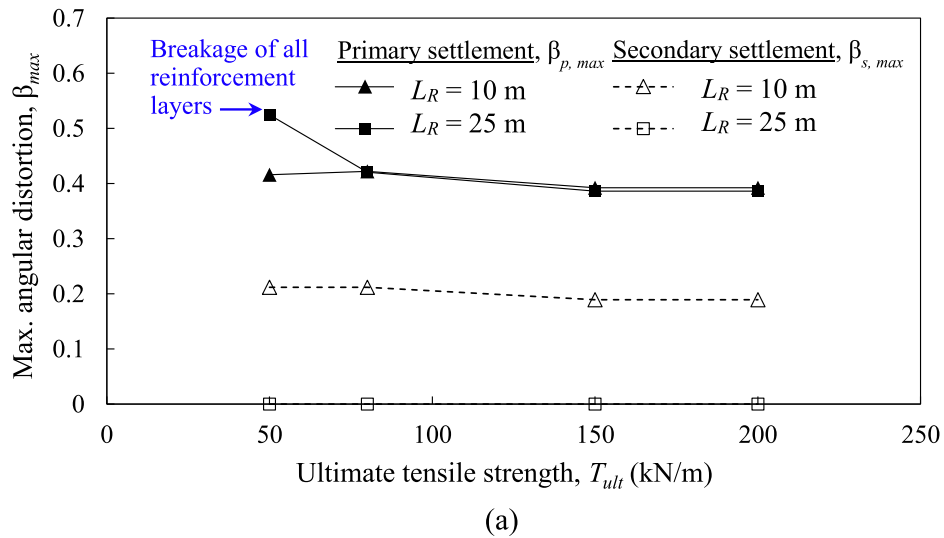
Fig. 17. Influence of reinforcement ultimate tensile strength on: (a) maximum angular distortion; (b) maximum reinforcement tensile strain at Layer 1 at $S = 1.0$ m.

Table 4
The corresponding fault offset when reinforcement breakage occurred.

L_R (m)	T_{ult} (kN/m)	Reinforcement breakage occurred at		
		Layer 1 (Bottom layer)	Layer 2 (Middle layer)	Layer 3 (Top layer)
10	50	$S = 0.2$ m	$S = 0.4$ m	–
10	80	$S = 0.5$ m	$S = 0.8$ m	–
10	150	–	–	–
10	200	–	–	–
25	50	$S = 0.2$ m	$S = 0.5$ m	$S = 0.7$ m
25	80	$S = 0.4$ m	$S = 0.8$ m	–
25	150	–	–	–
25	200	–	–	–

changes in input or output values are calculated in reference to the baseline case, which is located at the center of the figure. The slope of each line represents the degree of influence of the input parameters on β_{max} and ε_{max} values; the line with a steep slope has a large influence on β_{max} and ε_{max} values.

Fig. 22a shows the influence of all soil and reinforcement parameters on β_{max}. The S_v has a positive correlation with β_{max}, and the other soil

and reinforcement parameters have negative correlations with β_{max}. Among all the parameters, H, J_{50}, and S_v exert the most influence on β_{max}. The β_{max} value decreases by 12.5% and 5.6% when H and J_{50} decrease by 33% and 50% on the basis of the baseline case, respectively. Besides, the β_{max} value increases by 20.7% when S_v increases by 50% in comparison with the baseline case. Notably, significant reinforcement pullout occurs in the case of an excessively short reinforcement or a thin
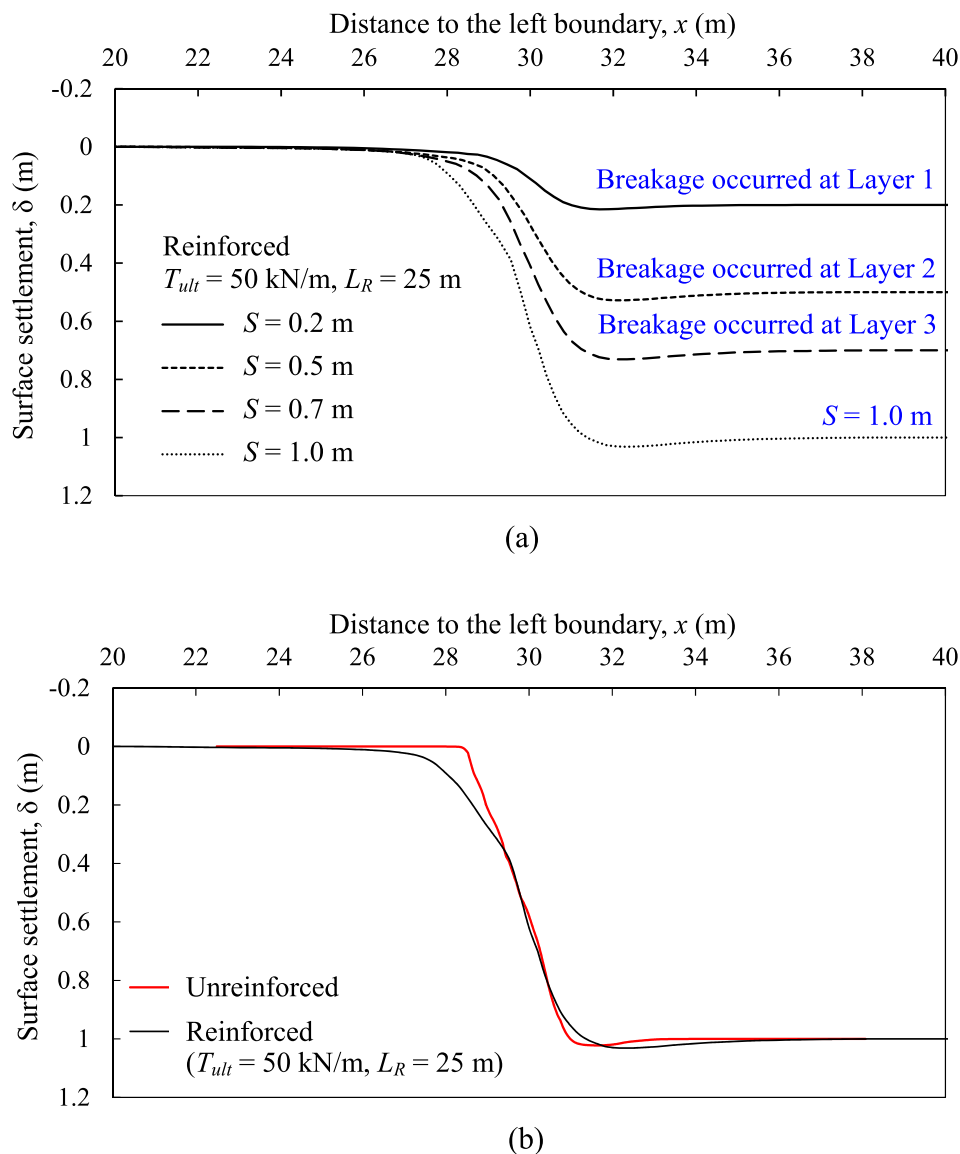
Distance to the left boundary, x (m)

Breakage occurred at Layer 1

Breakage occurred at Layer 2

Breakage occurred at Layer 3

$S = 1.0$ m

Reinforced
$T_{ult} = 50$ kN/m, $L_R = 25$ m
—— $S = 0.2$ m
------ $S = 0.5$ m
– – – $S = 0.7$ m
············ $S = 1.0$ m

(a)

Distance to the left boundary, x (m)

—— Unreinforced
—— Reinforced
($T_{ult} = 50$ kN/m, $L_R = 25$ m)

(b)

Fig. 18. Ground surface settlement profile for the case of reinforcement with low ultimate tensile strength: (a) at various fault offset; (b) compared with unreinforced foundation and at $S = 1.0$ m.

soil foundation, and reinforcement breakage occurs in the case of a reinforcement with a low ultimate tensile strength. Under these circumstances, β_{max} values could significantly increase by 40%.

Fig. 22b shows the influence of all soil and reinforcement parameters on ε_{max}. All soil and reinforcement parameters, except for J_{50}, have positive correlations with ε_{max}. Among all the parameters, H and J_{50} have considerable effects on ε_{max}, and R_{inter} within the range of typical input values has the most minor effect on ε_{max}. The ε_{max} value increases by 13% and 37% as H increases by 33% and J_{50} decreases by 50%, respectively. As indicated in Fig. 22b, reinforcement breakage and significant reinforcement pullout could limit the development of the reinforcement tensile strain; consequently, ε_{max} values could decrease by up to 60% under these circumstances.

4. Design method

This section presents the design methods for determining the reinforcement length (against significant pullout) and failure strain (against breakage). Moreover, multiple regression analyses were performed using the data from the parametric study. Regression equations were established for predicting ε_{max} and ε_{max} values under various soil and

reinforcement parameters and fault displacement.

4.1. Design of reinforcement length against significant pullout

As described in the previous section, the occurrence of significant reinforcement pullout in the top reinforcement layer may cause considerable high $\beta_{p,max}$ and $\beta_{s,max}$ values. In general, the reinforcement should have sufficient length to prevent significant pullout. Fig. 23 shows the determination of the fault influence length L_I at the free field ground surface (i.e., unreinforced foundation); the results are used to evaluate whether the reinforcement length is sufficient against significant reinforcement pullout. L_I is defined as the horizontal distance between the outcrops of two shear ruptures (i.e., SR1 and SR2). As illustrated in Fig. 23a, SR1 has an inclination angle α, which conforms approximately to the dip angle of the fault. SR2 has an inclination angle following the Rankine's theoretical active failure plane (i.e., $45° + \phi'/2$), as active soil failure occurs when the hanging wall is moved apart from the footwall. In Fig. 22b, $L_I = 4.83$ m, as obtained from the FE analysis of a 3-m-thick unreinforced foundation at $S = 1$. As mentioned in Section 3.1, the excessively short reinforcement in the case of $L_R = 5$ m yields high $\beta_{p,max}$ and $\beta_{s,max}$ values at $S = 1$ m due to the
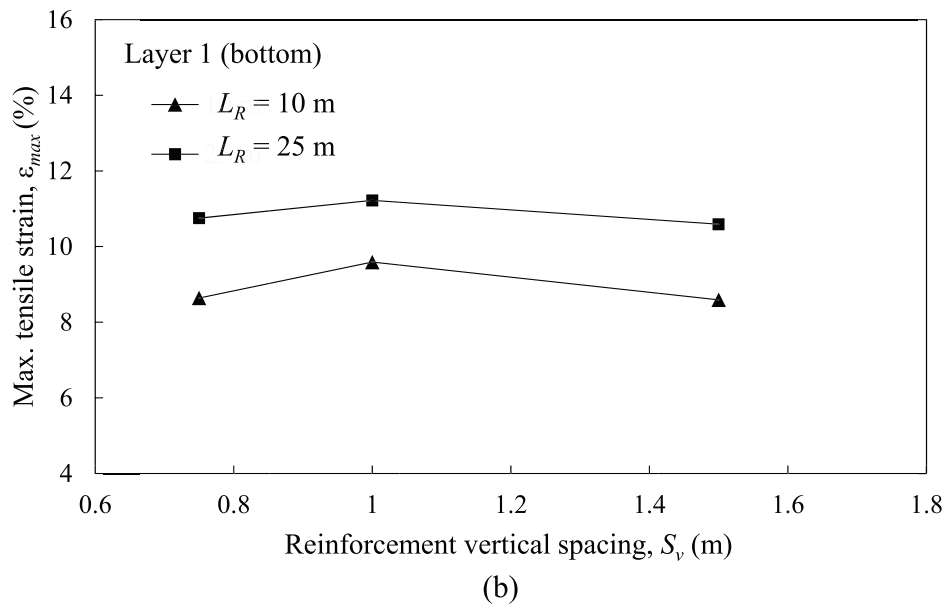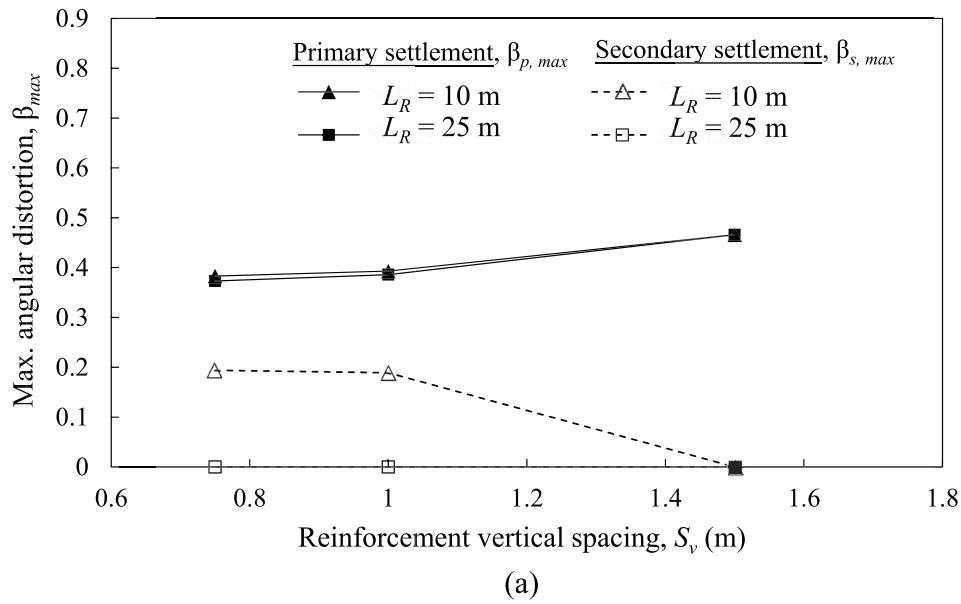
(a)

(b)

Fig. 19. Influence of reinforcement vertical spacing on: (a) maximum angular distortion; (b) maximum reinforcement tensile strain at Layer 1 at $S = 1.0$ m.

occurrence of significant reinforcement pullout. A comparison of L_R and L_I values reveals that L_R (=5 m) is approximately equal to L_I (=4.83 m), meaning that the entire reinforcement length is almost enclosed within the fault-induced active failure wedge; thus, the reinforcement has insufficient anchorage length.

Fig. 24a shows the numerical results of L_I for various H and S values. L_I increases as H and S increase. Using the data points from Fig. 24a, the relationships between the normalized influence length (L_I/H) and the fault displacement ratio (S/H) are shown in Fig. 23b. The regression equation is as follows:

$$\frac{L_I}{H} = 0.42 \times \ln\left(\frac{S}{H}\right) + 2.1 \tag{6}$$

For comparison, the theoretical solution derived based on the geometry of the active failure wedge (illustrated in Fig. 23a) is also provided in Fig. 24b. At a given S/H, the normalized L_I determined from FE analysis is higher than that in the theoretical solution. This is because the actual SR1 is a curve that slightly bends outward at the shallow

depth (Bray, 2009; Loukidis et al., 2009; Bray et al., 1994). The theoretical solution, in which SR1 is assumed to be a straight line, hence underestimates L_I.

According to the aforementioned discussion, when the reinforced foundation is subjected to normal fault movement, L_R should be longer than L_I to ensure adequate reinforcement anchorage against significant pullout. The design of reinforcement length L_R against significant pullout is proposed as

$$L_R = FS_{sp} \times L_I \tag{7}$$

where FS_{sp} is the required factor of safety against significant pullout, and L_I is the fault influence length at the free field ground surface.

4.2. Design of reinforcement failure strain against breakage

As discussed in the previous section, when the reinforcement has a low ultimate tensile strength, reinforcement breakage could occur, and the reinforcing function of the reinforcement is lost, leading to an
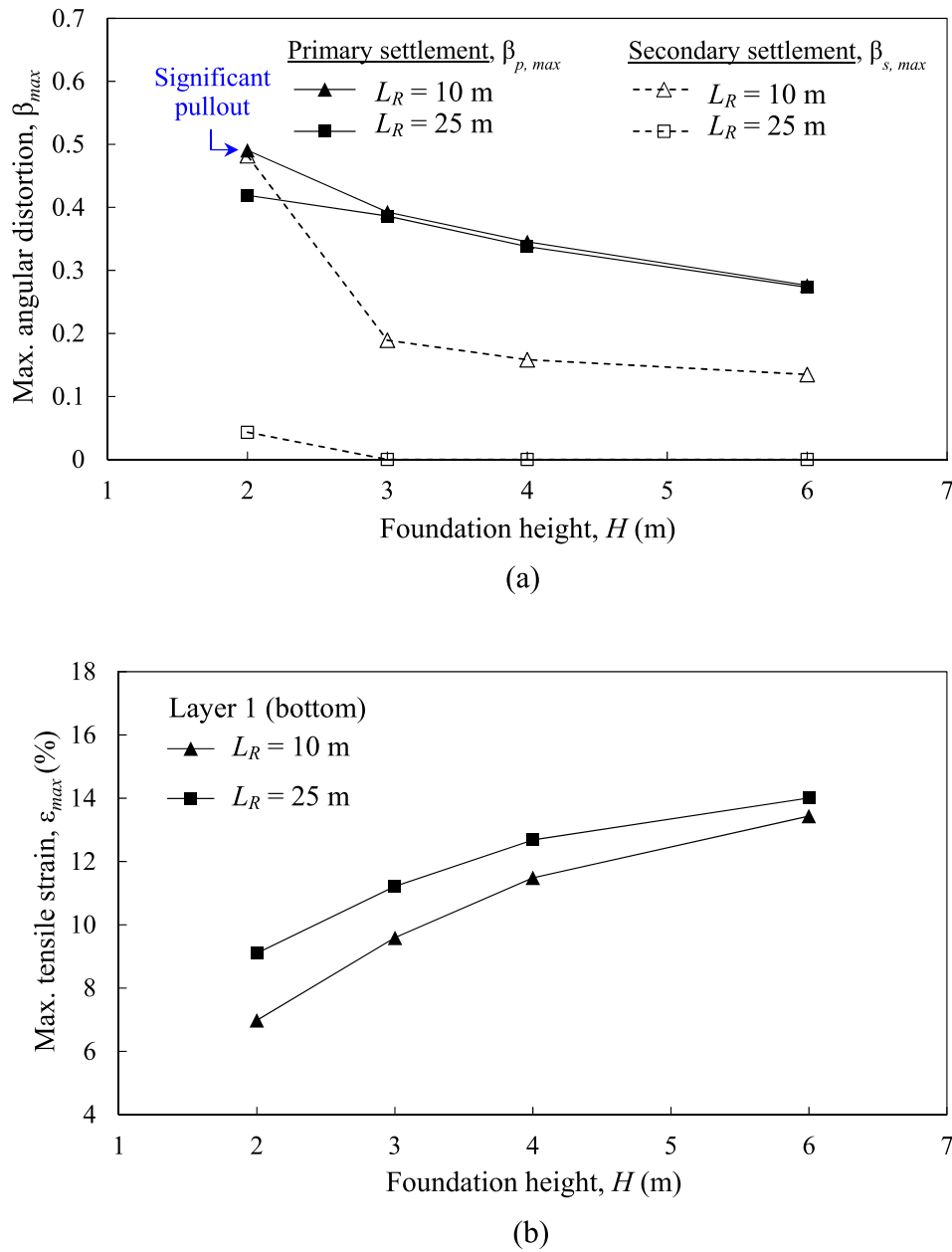
Fig. 20. Influence of foundation height on: (a) maximum angular distortion; (b) maximum reinforcement tensile strain at Layer 1 at $S = 1.0$ m.

increase in β_{max} at the ground surface. Particularly, if all the reinforcement layers are ruptured as fault displacement increases, β_{max} becomes close to that of the unreinforced foundation. In general, the reinforcement should have sufficient ultimate tensile strength to prevent reinforcement breakage. When the reinforced foundation is subjected to normal fault movement, ε_f (or T_{ult}) should be larger than ε_{max} (or T_{max}), which is possibly produced in the reinforcement with fault displacement.

Because the fault-induced ground deformation is a displacement-driven boundary problem, the prediction method for ε_{max} cannot be easily established just based on force-equilibrium or limit equilibrium approaches without considering the strain compatibility between soil and reinforcement. In this paper, multiple regression analyses are performed to analyze the FE results of the parametric study, excluding the cases with reinforcement breakage or significant pullout because the design of these failure cases should be avoided. A regression equation is established to predict the ε_{max} value under various soil and reinforcement parameters and fault displacement, and the equation is expressed as

$$\varepsilon_{max} = 63.88 \times \left(\frac{S}{H}\right)^{0.473} \left(\frac{L_R}{H}\right)^{0.248} \left(\frac{J_{50}}{\gamma S_v H}\right)^{-0.561} \left(\frac{T_{ult}}{\gamma S_v H}\right)^{0.020} \left(\frac{z}{H}\right)^{0.534} \quad (8)$$

where γ is the soil unit weigh, S_v is the vertical spacing of reinforcement, z is the depth of the reinforcement layer, and other parameters have been defined previously. Equation (8) contains five dimensionless quantities: normalized fault offset S/H, normalized reinforcement length L_R/H, normalized reinforcement stiffness $J_{50}/\gamma S_v H$, normalized reinforcement ultimate tensile strength $T_{ult}/\gamma S_v H$, and normalized reinforcement depth z/H. Among all quantities, S/H, $J_{50}/\gamma S_v H$, and z/H have high influence on the ε_{max} value, as these quantities have high positive or negative exponent values. Fig. 25 presents a comparison of ε_{max} obtained from FE analyses in the parametric study and that calculated using Eq. (8). The proposed regression equation can generate favorable prediction results for ε_{max} with $R^2 = 0.916$.

According to the aforementioned discussion, the design of rein-
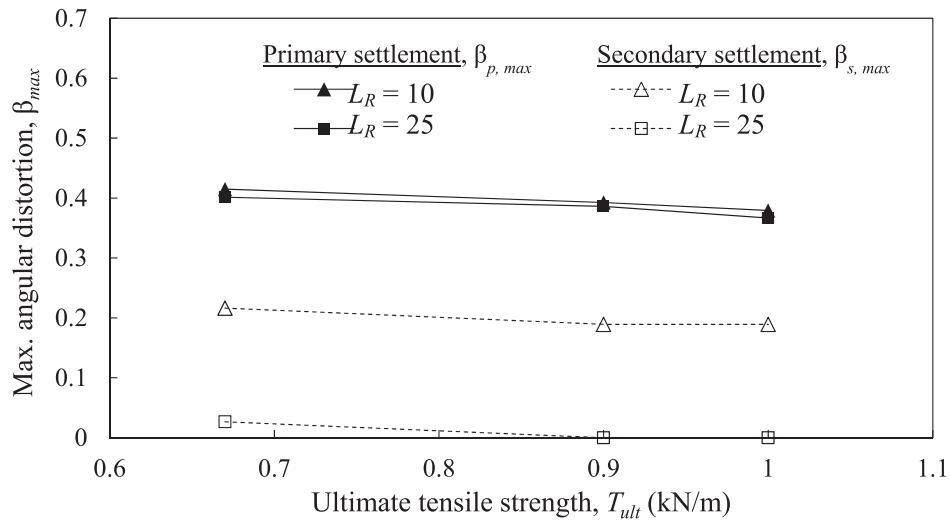
(a)
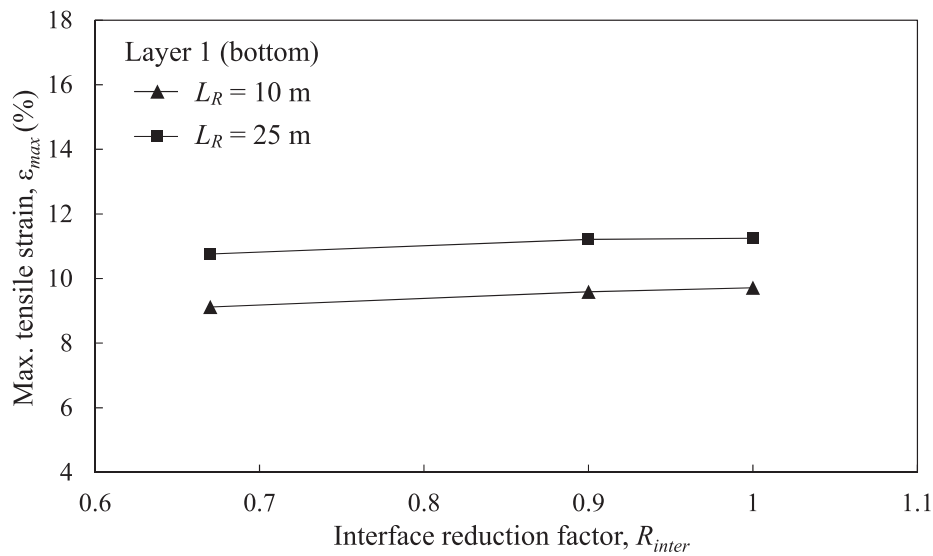
(b)

Fig. 21. Influence of soil-reinforcement interface property on: (a) maximum angular distortion; (b) maximum reinforcement tensile strain at Layer 1 at $S = 1.0$ m.

forcement failure strain ε_f against reinforcement breakage is proposed as

$$\varepsilon_f = FS_{br} \times \varepsilon_{max} \tag{9}$$

where FS_{br} is the required factor of safety against reinforcement breakage, and ε_{max} is the mobilized maximum tensile strain in the reinforcement layer.

4.3. Prediction of maximum angular distortion

Multiple regression analyses, as described previously, are also performed to establish the regression equation for predicting the β_{max} value with various soil and reinforcement parameters and fault displacement. The regression equation for predicting β_{max} is expressed as follows:

$$\beta_{max} = 1.313 \times \left(\frac{S}{H}\right)^{0.787} \left(\frac{L_R}{H}\right)^{-0.020} \left(\frac{J_{50}}{\gamma S_v H}\right)^{-0.116} \left(\frac{T_{ult}}{\gamma S_v H}\right)^{0.044} \tag{10}$$

Different from Eq. (8), the dimensionless quantity z/H is not included in Eq. (10) because β_{max} is obtained from the ground surface ($z = 0$).

Among all quantities, S/H has a high positive and $J_{50}/\gamma S_v H$ has a high negative influence on β_{max}. Fig. 26 presents a comparison of β_{max} obtained from FE analyses in the parametric study and that calculated using Eq. (10). Fig. 26 shows that β_{max} can be accurately predicted using the proposed regression equation with $R^2 = 0.99$. For comparison, Fig. 25 also includes the experimental results of the model and field tests on GRS foundations subjected to differential ground movement that have been reported in the literature (Yang et al., 2020; Hung et al., 2017; Ohta et al., 2013). The test conditions and material parameters of these studies are summarized in Table 5. The comparison results show the measured β_{max} from the experimental tests reported in the literature has satisfactory agreement with the predicted β_{max} calculated using Eq. (10), which confirms the validity of the proposed regression equation for the prediction of β_{max}.

Finally, the design of reinforced foundation subjected to normal faulting should satisfy the following criterion:

$$\beta_{max} < \beta_{allow} \tag{11}$$

Fig. 22. Results of sensitivity assessment: (a) maximum angular distortion; (b) maximum reinforcement tensile strain at $S = 1$.
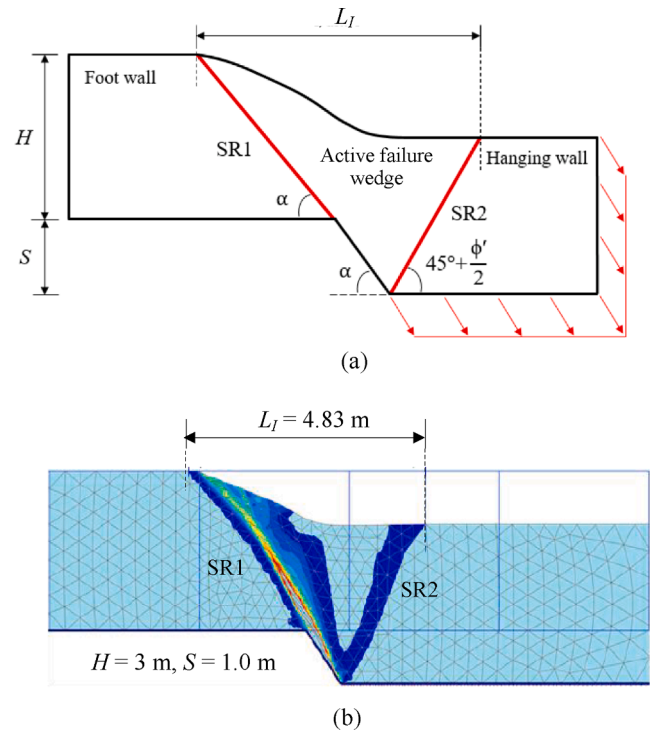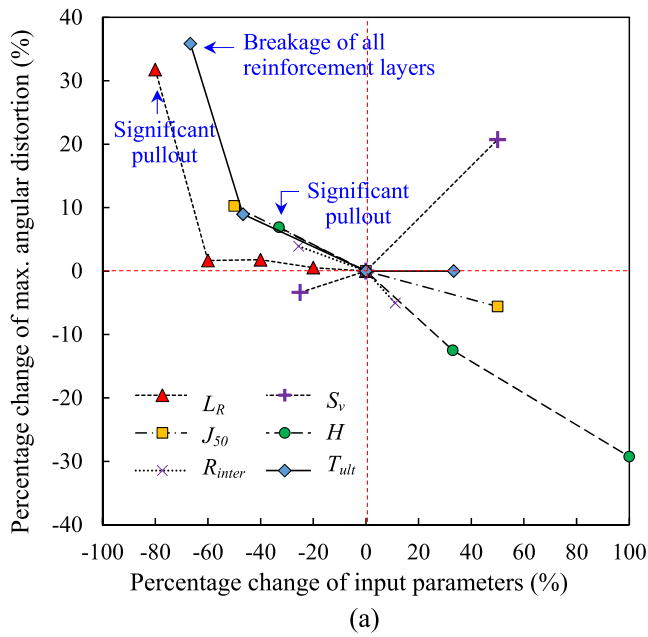

Fig. 23. Determination of fault influence length at the free field ground surface: (a) illustration; (b) FE result at $S = 1$ m.

5. Conclusions

A series of FE analyses were performed to investigate the performance and reinforcing mechanisms of GRS foundations subjected to normal fault movement. A parametric study was conducted to quantitatively evaluate the influence of soil and reinforcement parameters on the effectiveness of reinforced foundations. Design methods were developed for determining the reinforcement length (against significant pullout) and failure strain (against breakage), and regression equations for predicting β_{max} and ε_{max} induced by normal fault movement were established. On the basis of the numerical results, the key findings of the study are as follows:

- The FE analysis for modeling the reinforced foundation subjected to normal fault movement was validated using the model test results of unreinforced and reinforced foundations and a reinforced foundation with short reinforcement.
- This study demonstrated that the reinforced foundation is an effective mitigation measure for surface faulting hazards as the inclusion of a reinforcement can considerably reduce β_{max} at the ground surface.
- Two main reinforcing mechanisms, the tensioned membrane and shear rupture interception effects, were identified. For the tensioned membrane effect, the reinforcement caused the fault-induced ground movement to spread across a wider zone, resulting in a reduction in β_{max} at the ground surface. For the shear rupture interception effect, the reinforcement intercepted the upward propagation of a shear rupture, which prevented shear rupture breakthrough at the ground surface and caused a distinct surface fault rupture.
- The results of the parametric study showed that reinforcement pullout in the top reinforcement layer could occur in the case of the short reinforcement. Due to the impact of reinforcement pullout, the shear rupture propagated upward and passed through one end of the reinforcements, resulting in the development of a secondary settlement at the ground surface.
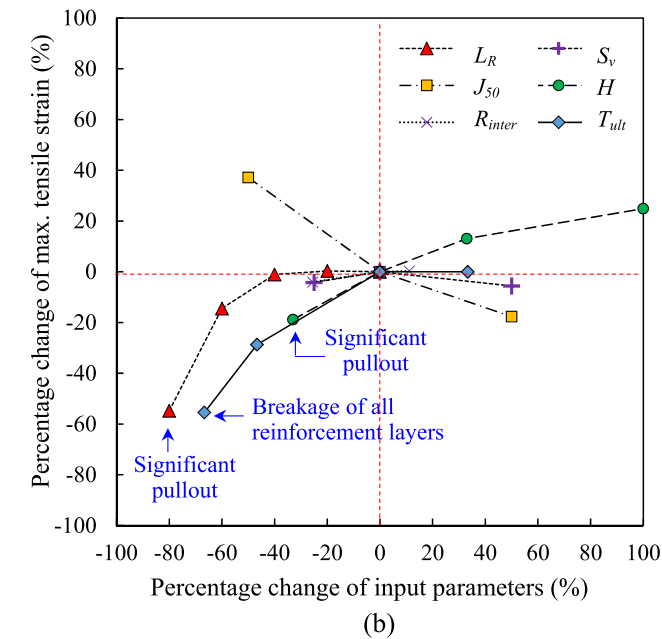
where β_{max} is the maximum angular distortion at the ground surface, and β_{allow} is the allowable angular distortion specified for a superstructure overlying the reinforced foundation. Multiple β_{allow} values can be set up based on various performance-based criteria. For instance, for the serviceability limit state (i.e., normal conditions), design guidelines (Elias et al., 2001; Wu et al., 2006; Holtz et al., 1998) suggest that β_{allow} values for GRS walls should be 1/200 for modular block walls and 1/50 for wrapped face walls. For reparability or the ultimate limit state under extreme conditions, β_{allow} values can be adopted from the relevant studies. Based on full-scale test results, Kost et al. (2014) reported that GRS walls with modular blocks had local failure (severely distressed, and several diagonal cracks developed) as the applied angular distortion at the ground reached 0.345.
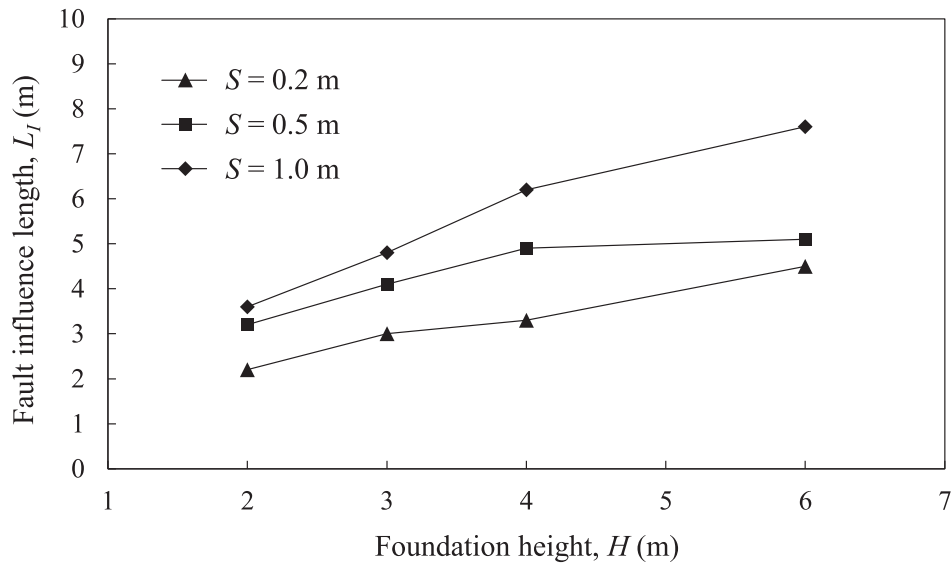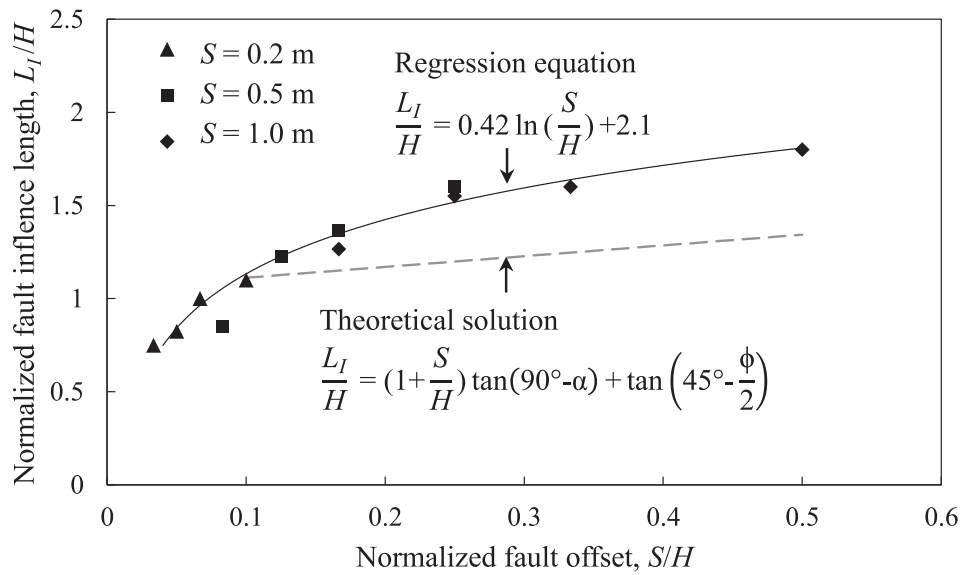
Fig. 24. Evaluation of fault influence length: (a) FE results for various fault offset and foundation height; (b) regression results and comparison with theoretical solution.

- The results of the parametric study also showed that reinforcement breakage could occur in the cases of the reinforcement with a low ultimate tensile strength. Due to the impact of reinforcement breakage, the reinforcing function of reinforcement layers was lost, resulting in substantial increases in β_{max}, which became close to that of the unreinforced foundation.
- The sensitivity assessment results showed that among all the parameters, the H, J_{50}, and S_v had considerable influence on β_{max} and ε_{max}. Notably, significant reinforcement pullout occurred in the case of the excessively short reinforcement or thin soil foundation, and reinforcement breakage occurred in the case of the reinforcement with a low ultimate tensile strength. Under these circumstances, β_{max} values significantly increased by 40%, and ε_{max} values decreased by 60%.
- The design methods for determining the reinforcement length and failure strain were proposed. To ensure adequate reinforcement

anchorage against significant pullout, the reinforcement length should be longer than the fault influence length at the free field ground surface. The reinforcement failure strain should be larger than the mobilized maximum reinforcement tensile strain to prevent reinforcement breakage.

- A regression equation for predicting β_{max} was established through multiple regression analyses, and the equation was validated by the experimental results of model and field tests on GRS foundations subjected to differential ground movement that have been reported in the literature. For the design of the reinforced foundation subjected to normal faulting, β_{max} should be lower than β_{allow}, where β_{allow} is the allowable angular distortion specified for a superstructure overlying the reinforced foundation, which can be set up based on various performance-based criteria.

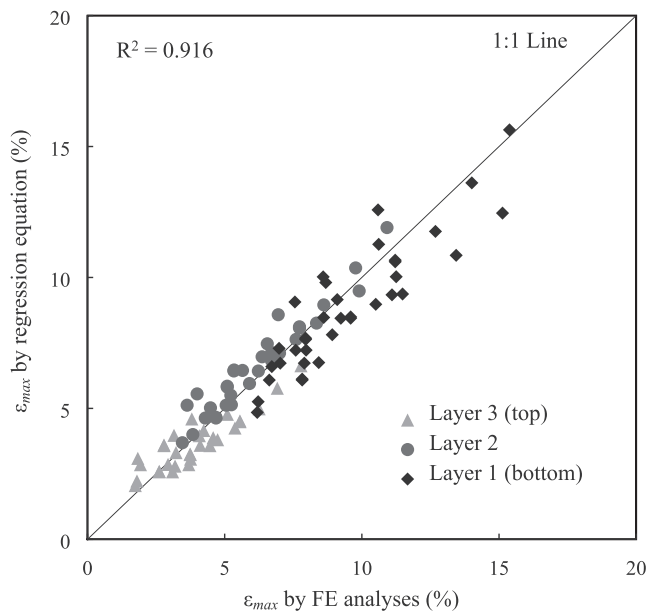The proposed regression equations are only applicable to reinforced

Fig. 25. Comparison of maximum reinforcement tensile strain obtained by FE analyses and regression equation.
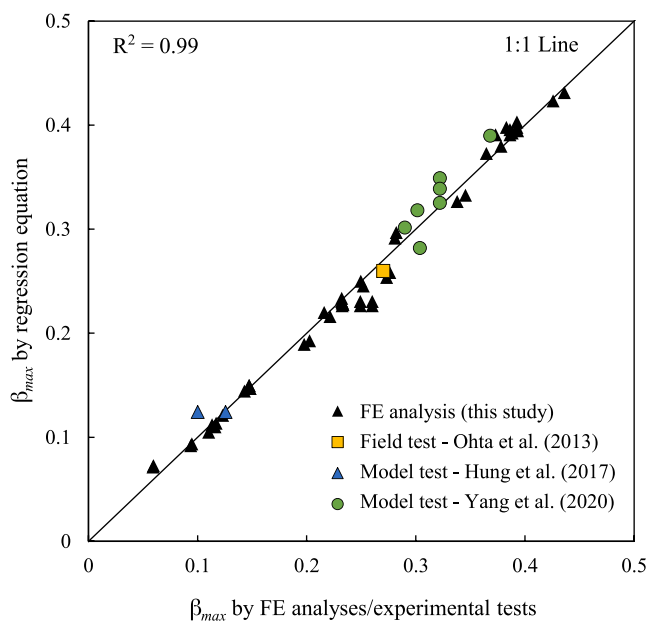

Fig. 26. Comparison of maximum angular distortion obtained by FE analyses, regression equation, and experimental tests reported in the literature.

foundations under soil and reinforcement parameters and fault displacement within the range of the parametric study. Extrapolation of the regression equations using the input parameters out of the range of the parametric study may lead to an incorrect predicted result. In addition, this study focused on the performance of GRS foundations subjected to normal fault movement. The impacts of various fault types (e.g., a reverse or thrust fault), external loadings, and the foundation–superstructure interaction were not evaluated and suggested to be investigated in future studies.

CRediT authorship contribution statement

Jung Chiang: Software, Formal analysis, Data curation, Writing – original draft. **Kuo-Hsin Yang:** Conceptualization, Methodology,

Table 5
Summary of test conditions and parameters of GRS foundations subjected to ground movement from the past studies.

Properties	Values		
	Yang et al. (2020) [a]	Hung et al. (2017)	Ohta et al. (2013)
Model			
Model scale	Reduced scale	Reduced scale	Full scale
Soil type	Sand (SP)	Sand (SP)	Crushed stone
Foundation height, H (m)	0.2–0.3 (3–4.5)	0.3	2
Fault offset, S (m)	0.06 (0.9)	0.05	0.55
Reinforcement			
Reinforcement type	Geotextile [b]	Geogrid [c]	Geogrid [c]
Number of layers, n	1–6	4	4
Reinforcement Length, L_R (m)	1 (15)	1.2	10
Ultimate tensile strength, T_{ult} (kN/m)	0.7 (157.5)	200	200
Stiffness, J_{50} (kN/m)	5.5–16.5 (1231–3693)	4400	4400

[a] values in parenthesis are in prototype scale.
[b] fixed at both ends to prevent pullout.
[c] confined by rigid steel anchors.

Investigation, Writing – original draft, Supervision, Project administration, Funding acquisition. **Yu-Hsuan Chan:** Software, Formal analysis, Data curation, Visualization. **Chung-Lu Yuan:** Conceptualization, Resources.

Declaration of Competing Interest

The authors declare that they have no known competing financial interests or personal relationships that could have appeared to influence the work reported in this paper.

Declaration of Competing Interest

The authors declare that they have no known competing financial interests or personal relationships that could have appeared to influence the work reported in this paper.

References

Allen, T.M., Bathurst, R.J., Holtz, R.D., Walters, D., Lee, W.F., 2003. A new working stress method for prediction of reinforcement loads on geosynthetic walls. Can. Geotech. J. 40 (5), 976–994.

Anastasopoulos, I., Gazetas, G., Bransby, M.F., Davies, M.C.R., El Nahas, A., 2007. Fault rupture propagation through sand: finite-element analysis and validation through centrifuge experiments. J. Geotech. Geoenviron. Eng., ASCE 133 (8), 943–958.

Anastasopoulos, I., Gazetas, G., Bransby, M.F., Davies, M.C., El Nahas, A., 2009. Normal fault rupture interaction with strip foundations. J. Geotech. Geoenviron. Eng., ASCE 135 (3), 359–370.

Ardah, A., Abu-Farsakh, M.Y., Voyiadjis, G.Z., 2018. Numerical evaluation of the effect of differential settlement on the performance of GRS-IBS. Geosynthetics Int. 25 (4), 427–441.

Ashtiani, Mehdi, Ghalandarzadeh, Abbas, Mahdavi, Mehdi, Hedayati, Majid, 2018. Centrifuge modeling of geotechnical mitigation measures for shallow foundations subjected to reverse faulting. Can. Geotech. J. 55 (8), 1130–1143.

Bolton, M.D., 1986. The strength and dilatancy of sands. Geotechnique 36 (1), 65–78.

Bray, J.D., 2001. Developing mitigation measures for the hazards associated with earthquake surface fault rupture. A Workshop on Seismic Fault-Induced Failures–Possible Remedies for Damage to Urban Facilities, Japan Society for Promotion of Science, University of Tokyo, Japan.

Bray, J.D., 2009. Earthquake surface fault rupture design considerations. In: Proceedings of the Sixth International Conference on Urban Earthquake Engineering, Tokyo, Japan, pp. 37–45.

Bray, J.D., Ashmawy, A., Mukhopadhyay, G., Gath, E.M., 1993. Use of geosynthetics to mitigate earthquake fault rupture propagation through compacted fill. In: Proceedings of the Geosynthetics'93 Conference, Vancouver, Canada, 1, 379-392.

Bray, Jonathan D., Seed, Raymond B., Cluff, Lloyd S., Seed, H. Bolton, 1994. Earthquake fault rupture propagation through soil. J. Geotech. Eng., ASCE 120 (3), 543–561.

Brinkgreve, R.B.J., Kumarswamy, S., Swolfs, W.M., Zampich, L., Ragi Manoj, N., 2019. PLAXIS 2D Manual, Plaxis bv, Bentley Systems, Inc., Netherlands.

Chen, Y.G., Chen, W.S., Lee, J.C., Lee, Y.H., Lee, C.T., 2001. Surface rupture of 1999 Chi-Chi earthquake yields insights on active tectonics of central Taiwan. Bull. Seismol. Soc. Am. 91 (5), 977–985.

Elias, V., Christopher, B.R., Berg, R., 2001. Mechanically Stabilized Earth Walls and Reinforced Soil Slopes Design and Construction Guidelines. National Highway Institute, Federal Highway Administration, Washington, D.C.

Faccioli, E., Anastasopoulos, I., Gazetas, G., Callerio, A., Paolucci, R., 2008. Fault rupture–foundation interaction: selected case histories. Bull. Earthq. Eng. 6 (4), 557–583.

Fadaee, Meysam, Ezzatyazdi, Pedram, Anastasopoulos, Ioannis, Gazetas, George, 2016. Mitigation of reverse faulting deformation using a soil bentonite wall: dimensional analysis, parametric study, design implications. Soil Dyn. Earthq. Eng. 89, 248–261.

Garcia, F.E., Bray, J.D., 2019a. Discrete element analysis of earthquake fault rupture-soil-foundation interaction. J. Geotech. Geoenviron. Eng., ASCE 145 (9), 04019046.

Garcia, F.E., Bray, J.D., 2019b. Discrete-element analysis of influence of granular soil density on earthquake surface fault rupture interaction with rigid foundations. J. Geotech. Geoenviron. Eng., ASCE 145 (11), 04019093.

Gazetas, G., Pecker, A., Faccioli, E., Paolucci, R., Anastasopoulos, I., 2008. Preliminary design recommendations for dip-slip fault–foundation interaction. Bull. Earthq. Eng. 6 (4), 677–687.

Giroud, J.P., Bonaparte, R., Beech, J.F., Gross, B.A., 1990. Design of soil layer-geosynthetic systems overlying voids. Geotext. Geomembr. 9 (1), 11–50.

Hatami, Kianoosh, Bathurst, Richard J., 2006. Numerical model for reinforced soil segmental walls under surcharge loading. J. Geotech. Geoenviron. Eng., ASCE 132 (6), 673–684.

Hung, H.M., Kuwano, J., Tachibana, S., 2017. Effect of lateral boundary condition on confined-reinforced earth subjected to differential settlement. Int. J. GEOMATE 13 (38), 149–156.

Holtz, R.D., Cristopher, B.R., Berg, R.R., 1998. Geosynthetic design and construction guidelines. FHWA HI-95-038, National Highway Institute Federal Highway Administration (FHWA), McLean, Virginia.

Jiang, Kang, Gao, Fu Liang, Fang, Wei, 2012. Treatment mechanism research on the roadbed widening with geosynthetics. Appl. Mech. Mater. 204-208, 1789–1793.

King, Louis, Bouazza, Abdelmalek, Gaudin, Christophe, O'Loughlin, Conleth D., Bui, Ha H., 2019. Behavior of geosynthetic-reinforced piled embankments with defective piles. J. Geotech. Geoenviron. Eng., ASCE 145 (11), 04019090. https://doi.org/10.1061/(ASCE)GT.1943-5606.0002125.

Kost, A.D., Filz, G.M., Cousins, T., Brown, M.C., 2014. Full-scale investigation of differential settlements beneath a GRS bridge. Transport. Res. Rec.: J. Transport. Res. Board 2462 (1), 28–36.

Lade, P.V., Lee, K.L., 1976. Engineering Properties of Soils. Report UCLA-ENG-7652, University of California, Los Angeles, California.

Lazarte, C.A., Bray, J.D., Johnson, A.M., Lemmer, R.E., 1994. Surface breakage of the 1992 Landers earthquake and its effects on structures. Bull. Seismol. Soc. 84 (3), 547–561.

Loli, Marianna, Kourkoulis, Rallis, Gazetas, George, 2018. Physical and numerical modeling of hybrid foundations to mitigate seismic fault rupture effects. J. Geotech. Geoenviron. Eng., ASCE 144 (11), 04018083. https://doi.org/10.1061/(ASCE)GT.1943-5606.0001966.

Loukidis, Dimitrios, Bouckovalas, George D., Papadimitriou, Achilleas G., 2009. Analysis of fault rupture propagation through uniform soil cover. Soil Dynamics and Earthquake Engineering 29 (11-12), 1389–1404.

Marachi, N., Duncan, J.M., Chan, C., Seed, H.B., 1981. Plane-strain testing of sand. In: Yong, R.N., Townsend, F.C. (Eds.), laboratory shear strength of soil, ASTM Special Technical Bulletin 740. American Society for Testing and Materials, West, Conshohocken, pp. 294–302.

Marx, D.H., Jacobsz, S.W., 2018. Optimal placement of reinforcement in piggyback landfill liners. Geotext. Geomembr. 46 (3), 327–337.

Moosavi, S.M., Jafari, M.K., 2012. Investigation of the Surface Fault Rupture Hazard Mitigation by Geosynthetics. In: Proceedings of the 15th World Conference on Earthquake Engineering, Lisbon, Portugal.

Oettle, Nicolas K., Bray, Jonathan D., 2013. Geotechnical mitigation strategies for earthquake surface fault rupture. J. Geotech. Geoenviron. Eng., ASCE 139 (11), 1864–1874.

Ohta, H., Ishigaki, T., Tatta, N., 2013. Retrofit technique for asphalt concrete pavements after seismic damage. In: Proceedings of 18th International Conference on Soil Mechanics and Geotechnical Engineering, Paris.

Rajesh, S., Viswanadham, B.V.S., 2012. Centrifuge modeling and instrumentation of geogrid-reinforced soil barriers of landfill covers. J. Geotech. Geoenviron. Eng., ASCE 138 (1), 26–37.

Rajesh, S., Viswanadham, B.V.S., 2015. Numerical simulation of geogrid-reinforced soil barriers subjected to differential settlements. Int. J. Geomech., ASCE 15 (4), 04014062. https://doi.org/10.1061/(ASCE)GM.1943-5622.0000405.

Rasouli, Habib, Fatahi, Behzad, 2019. A novel cushioned piled raft foundation to protect buildings subjected to normal fault rupture. Comput. Geotech. 106, 228–248.

Schanz, T., Vermeer, P.A., Bonnier, P.G., 1999. The hardening soil model-formulation and verification. Beyond 2000 in Computational Geotechnics – 10 Years of PLAXIS, Balkema, Rotterdam.

Stulgis, Richard P., Soydemir, Cetin, Telgener, Richard J., Hewitt, Robert D., 1996. Use of geosynthetics in 'piggyback landfills': a case study. Geotext. Geomembr. 14 (7-8), 341–364.

Talebi, Majid, Meehan, Christopher L., Leshchinsky, Dov, 2017. Applied bearing pressure beneath a reinforced soil foundation used in a geosynthetic reinforced soil integrated bridge system. Geotext. Geomembr. 45 (6), 580–591.

Wu, J.T.H, Lee, K.Z.Z., Helwany, S., and Ketchart, K. (2006). Design and construction guidelines for geosynthetic-reinforced soil bridge abutments with a flexible facing. National Cooperative Highway Research Program, Report 556, Washington D.C.

Xu, R., Fatahi, B., 2018. Geosynthetic-reinforced cushioned piles with controlled rocking for seismic safeguarding. Geosynthetics Int. 25 (6), 561–581.

Yang, K.H., Chiang, J., Lai, Z.W., Han, J., Lin, M.L., 2020. Performance of geosynthetic-reinforced soil walls across a normal fault. Geotext. Geomembr. 48 (3), 357–373.

Yang, K.H., Nguyen, T.S., Lee, Y.H., Leshchinsky, B., 2019. Performance and design of geosynthetic-reinforced soil slopes against rainfall: considering regional hydrological conditions. Geosynthetics Int. 26 (5), 451–473.